

1 Quantifying aerosol direct radiative effect with MISR observations: I.

2 TOA albedo change by aerosols based on land surface types

3
4
5
6 Yang Chen^{1,3}

7 Qinbin Li¹

8 Ralph A. Kahn^{1,2}

9 James T. Randerson³

10 David J. Diner¹

11
12
13
14
15
16 ¹Jet Propulsion Laboratory, California Institute of Technology, Pasadena, CA

17 ²Now at NASA Goddard Space Flight Center, Greenbelt, MD

18 ³Department of Earth System Science, University of California, Irvine, CA

Abstract

Using internally-consistent albedo, aerosol, cloud and surface data from the Multi-angle Imaging SpectroRadiometer (MISR) instrument onboard the Terra satellite, top-of-atmosphere (TOA) spectral albedo change ($d\alpha$) in the presence of aerosols over land is estimated and its dependence on aerosol and surface properties is analyzed. Linear regressions between spectral TOA albedo and aerosol optical depth (AOD) for different surface types are examined to derive the aerosol-free TOA albedo. MISR surface BiHemispherical Reflectance (BHR) values are used to differentiate surface types. We find relatively high correlations between spectral TOA albedo and AOD for BHR-stratified data in $2^\circ \times 2^\circ$ grid cells. The global mean values of cloud-free $d\alpha$ over land for June-September 2007 are estimated to be 0.018 ± 0.003 (blue), 0.010 ± 0.003 (green), 0.007 ± 0.003 (red), and 0.008 ± 0.006 (NIR). Individual regions show large variations from these values. Global patterns of $d\alpha$ are determined mainly by AOD and aerosol radiative efficiency. Large positive values of $d\alpha$ are observed over regions with high aerosol loading and large single-scattering albedo (SSA), where the aerosol scattering effect is dominant. The presence of light absorbing aerosols reduces aerosol radiative efficiency and $d\alpha$. Surface reflectance influences both aerosol scattering and absorbing effects. Generally, the aerosol radiative efficiency decreases with increasing BHR. We also examined $d\alpha$ – AOD correlations over different vegetation types. We find the smallest $d\alpha$ values are over needleleaf forests and shrublands, whereas the largest values are over cropland and barren regions. The aerosol radiative efficiencies are lowest over needleleaf forests and barren regions, and highest over grasslands and croplands.

43

44 1. Introduction

45 Aerosols, both natural and anthropogenic, perturb the radiative balance of Earth's atmosphere
46 directly by scattering and absorbing the solar irradiance [*Chylek and Coakley*, 1974; *Coakley et*
47 *al.*, 1983; *Charlson et al.*, 1990]. On a global average, anthropogenic aerosols exert a negative
48 radiative forcing, including a total aerosol direct radiative forcing of $-0.5 \pm 0.4 \text{ Wm}^{-2}$ [*IPCC*,
49 2007]. It partly offsets the positive radiative forcing caused by the post-industrial rise of carbon
50 dioxide ($1.66 \pm 0.17 \text{ Wm}^{-2}$, *IPCC* [2007]), though the spatial distributions of aerosol forcing is
51 very different. An accurate quantification of the aerosol direct radiative forcing is critical for the
52 interpretation of previous climate records and the projection of future climate change
53 [*Mishchenko et al.*, 2007; *Chylek et al.*, 2007].

54 Current estimates of the aerosol direct radiative forcing have large uncertainties [*IPCC*, 2007].
55 Aerosol particles have a variety of shapes, sizes, and chemical compositions, that directly affect
56 the aerosol optical properties and the ability of aerosols to change the climate [*Kaufman et al.*,
57 2002a]. Spatial and temporal distributions of aerosols are highly variable due to their diverse
58 sources and short lifetimes [*Quinn et al.*, 2000; *Quinn and Bates*, 2005]. Additionally, the land
59 surface is highly heterogeneous in reflecting and absorbing solar radiation at different
60 wavelengths [*Betts et al.*, 1996], which also impacts the aerosol effect on Earth's radiative
61 balance. Thus, estimating aerosol radiative forcing is more challenging than estimating the
62 radiative forcing due to well-mixed greenhouse gases.

63 A large portion of the uncertainty in quantifying aerosol direct radiative forcing results from poor
64 constraints on the aerosol shortwave direct radiative effect (SWDRE). In this paper, we use the
65 term aerosol radiative effect to represent the change in top-of-atmosphere (TOA) radiative fluxes

66 due to the presence of all aerosols (natural and anthropogenic), and distinguish this from aerosol
67 radiative forcing (the radiative effect of anthropogenic aerosols alone). The estimation of
68 SWDRE by all aerosol species is the basis for quantifying the direct radiative forcing by
69 anthropogenic aerosols. Therefore, a first step toward reducing the uncertainty range of aerosol
70 forcing is to improve the estimate of aerosol SWDRE.

71 Previously, a widely used approach for estimating the aerosol SWDRE is through chemical
72 transport and general circulation model simulations [e.g., *Hansen et al.*, 1998]. There are large
73 uncertainties in these model-based estimates as well as discrepancies among them, due to
74 incomplete knowledge of aerosol processes and assumptions made in the aerosol simulations [*Yu*
75 *et al.*, 2006; *Kinne et al.*, 2006]. Recently, much effort has also been made to assess the aerosol
76 radiative effect using measurements from ground based networks, satellite sensors, and intensive
77 aircraft field experiments [*Yu et al.*, 2006]. In particular, satellite remote sensing provides
78 frequent, global coverage of aerosol amount and type, as well as the TOA radiance distribution.
79 It thus offers a unique opportunity to constrain aerosol SWDRE [*Kaufman et al.*, 2002a;
80 *Anderson et al.*, 2005; *Diner et al.*, 2005].

81 Two approaches have been used to exploit satellite data in the calculation of aerosol SWDRE. In
82 the first approach, satellite aerosol observations are used to feed a radiative transfer model to
83 derive the aerosol radiative effect [e.g., *Yu et al.*, 2004; *Remer and Kaufman*, 2006]. The second
84 approach uses satellite observations directly without resorting to radiative transfer calculations.
85 In this case, the aerosol direct radiative effect is derived from satellite-observed changes in
86 broadband radiative flux due to the presence of aerosols in the atmosphere [*Christopher et al.*,
87 2000; *Loeb and Kato*, 2002; *Christopher and Zhang*, 2002; *Loeb and Manalo-Smith*, 2005].
88 However, the satellite-only approach has so far been limited primarily to over the oceans.

89 Application of this approach over land remains challenging mainly because of the large
90 uncertainty in aerosol retrievals over bright land surfaces, the large heterogeneity in land surface
91 reflectivity, and the difficulty to estimate the TOA radiative flux for aerosol-free scenes [*Loeb*
92 *and Kato*, 2002]. The Multi-angle Imaging SpectroRadiometer (MISR) aboard NASA's Terra
93 satellite provides more accurate aerosol optical depth (AOD) retrievals over land [*Abdou et al.*,
94 2005], as well as more information about aerosol properties [*Kahn et al.*, 2001], than are
95 obtained from single-angle, multi-spectral techniques. It thus has the potential to reduce aerosol
96 SWDRE uncertainties over land. Recently, *Patadia et al.* [2008] estimated aerosol SWDRE over
97 global land using merged Clouds and Earth's Radiant Energy System (CERES), Moderate
98 Resolution Imaging Spectroradiometer (MODIS), and MISR data. They obtained aerosol-free
99 TOA broadband flux through the regression between MISR single-band AOD and CERES
100 broadband flux for $0.5^{\circ} \times 0.5^{\circ}$ cloud-free regions.

101 In this study, we estimate the aerosol SWDRE on a global scale. Our approach is similar but
102 different in several important ways from that of *Patadia et al.* [2008]. First, we use MISR data
103 for aerosol properties, TOA albedo, surface optical properties, and cloud properties. The use of
104 internally consistent data should reduce systematic sampling biases that can occur when data
105 from different instruments are used. Second, we estimate the aerosol-free TOA albedo separately
106 for different land cover types within a region, thereby taking into account land surface
107 heterogeneity. Finally, we examine the relationship between the spectral TOA albedo and
108 spectral AOD, which may better represent non-linear wavelength dependent effects.

109 This paper is the first in a two-part series. In Part I, we examine the TOA albedo change due to
110 the presence of aerosols over land by analyzing four months of MISR data for June-September
111 2007. During this period, intense wildfires were observed in Central Africa, North America,

South America, and Siberia [NASA/University of Maryland, 2002]. Large amounts of light absorbing aerosols, including black carbon, were emitted from the wildfires. We focus on investigating how the aerosol amount, aerosol optical properties and land surface type affect the spectral aerosol radiative effect. In Part II we will present a method for estimating aerosol broadband SWDRE over the globe. Multiple-year MISR data will be explored and seasonal and inter-annual variability of aerosol SWDRE will be examined.

Detailed descriptions of MISR data and the methodology used are presented in section 2. The global distribution of TOA albedo change due to aerosols, as well as its dependence on aerosol properties and surface type, are shown in section 3. We present an uncertainty analysis for these calculations in section 4. Summary and conclusions are given in section 5.

2. Data and Methodology

2.1 MISR data

The MISR sensor uses nine cameras pointed at fixed viewing angles (0° , $\pm 26.1^\circ$, $\pm 45.6^\circ$, $\pm 60.0^\circ$, $\pm 70.5^\circ$) to observe reflected and scattered sunlight in four spectral bands: 446 (blue), 558 (green), 672 (red), and 866 nm (near infrared, NIR) [Diner *et al.*, 1998]. The swath width is ~ 400 km, which provides global coverage in about nine days at the equator and two days near the poles.

MISR global retrievals of aerosols, TOA albedo, surface properties and cloud information are available since late February 2000. For the purpose of quantifying TOA albedo change by aerosols, four MISR level 2 products are used in this study (Table 1): the aerosol product (AS_Aerosol), the albedo product (TC_Albedo), the land surface product (AS_Land), and the classifier product (TC_Classifier).

134 We use the ‘best estimate optical depth’ from the MISR Level 2 Aerosol Product (Version 20),
135 which has a spatial resolution of $17.6 \times 17.6 \text{ km}^2$ [Diner *et al.*, 2001] and is reported at four
136 spectral bands as mentioned above. The uncertainties of MISR AOD have been assessed with
137 independent measurements. For example, Liu *et al.* [2004] estimated that the MISR AOD
138 retrieval error over land is approximately $0.04 + 0.18 \text{ AOD}$. Thus, for AOD values between 0.1
139 and 0.5 over land, the expected error in MISR AOD should be within 0.06-0.13. In comparison,
140 the error in the MODIS AOD retrieval over land had been estimated to be $0.05 + 0.2 \text{ AOD}$ [Chu
141 *et al.*, 2002]. Kahn *et al.* [2005] showed that about 2/3 of the MISR-retrieved AOD values fall
142 within $\pm 20\%$ of concurrent AERONET values. In particular, the MISR retrievals over desert and
143 coastal regions, where surface brightness and subpixel water contamination makes accurate
144 retrievals challenging, are in good agreement with AERONET [Abdou *et al.*, 2005; Martonchik
145 *et al.*, 2004]. Recently, Liu and Mishchenko [2008] compared coincident AOD measurements
146 from MISR and MODIS. They showed the agreement over the land is often poor and even
147 unacceptable. However, they acknowledged that their analysis cannot be used to determine
148 which retrieval is more accurate.

149 MISR also constrains aerosol Single Scattering Albedo (SSA) and Angstrom Exponent (AE).
150 SSA represents the relative importance of aerosol scattering and absorption, and AE contains
151 information about aerosol size. MISR aerosol retrieval method and its sensitivity to SSA have
152 been previously reported [Chen *et al.*, 2008; and references therein]. Uncertainties for AE and
153 SSA are difficult to estimate due to the lack of validation data. We are currently evaluating these
154 quantities by comparison to AERONET values. The challenge is that there are far fewer
155 AERONET particle property retrievals than AOD retrievals. Additionally, AERONET-derived
156 SSA is not a direct measurement and is subjected to many of the same uncertainties as the

satellite retrievals. In this study, we use MISR-derived SSA and AE to study how these aerosol optical properties influence the aerosol ability to modify TOA albedo.

Based on observed radiances, MISR generates several TOA albedo products [Diner *et al.*, 1999]. For the present study, we use the TOA local albedo, because it has the highest spatial resolution ($2.2 \times 2.2 \text{ km}^2$) among all albedo products. MISR assigns recorded upward radiances to the tops and sides of vertical columns, $2.2 \times 2.2 \text{ km}^2$ in horizontal extent, at a height given by the Reflecting Level Reference Altitude (RLRA) obtained from stereo-derived cloud top heights. The spectral TOA local albedos from the MISR Level 2 standard product are determined only from the top-leaving radiances. Because the side-leaving, upward radiances are not included, using these albedos would probably cause an underestimation of the aerosol radiative effect. In this study, we include the side contribution by adding back the un-obscured side-leaving, upward radiances stored in the MISR TOA Albedo product. The radiances from different cameras are weighted using pre-established solid angle weighting factors [Diner *et al.*, 1999]. To be compatible with the AOD product, we re-sampled the TOA local albedo (with side contribution included) to the $17.6 \times 17.6 \text{ km}^2$ resolution AOD grid. This method is similar to the standard process of deriving MISR restrictive albedo [Diner *et al.*, 1999]. The only difference is that we calculate the albedo for $17.6 \times 17.6 \text{ km}^2$ domains, whereas the MISR restrictive albedo was derived on $35.2 \times 35.2 \text{ km}^2$ domains. The TOA albedo and AOD for each cloud-free $17.6 \times 17.6 \text{ km}^2$ grid box are defined as a ‘data pair’, which will be subject to linear regression analysis as discussed in section 2.2.

In this study we use two different MISR products for cloud screening. In the base case calculation, we use the ‘SVM Cloud Confidence Level (CCL)’, which was derived using Support Vector Machine (SVM), a machine learning technique [Mazzoni *et al.*, 2007]. The MISR SVM

CCL product has a spatial resolution of $1.1 \times 1.1 \text{ km}^2$. The $17.6 \times 17.6 \text{ km}^2$ grid box is set to ‘cloudy’ if a single value of SVM CCL within the grid box is ‘highly likely’ or ‘likely’. This aggregation of confidence levels is conservative, to minimize the cloud contamination. All plots and tables shown in this paper are derived using SVM CCL cloud masks. As a sensitivity test, we also use the ‘Cloudy Clear Designation (CCD)’, which was used for determining the azimuthal model in the MISR TOA local albedo standard retrieval. Similarly, we assume a $17.6 \times 17.6 \text{ km}^2$ grid box to be cloudy if a single pixel within it is marked with a ‘cloudy’ CCD. The cloudy grid boxes are excluded from further calculations.

The MISR Surface product provides a number of parameters related to land surface properties, which can be used for stratifying by surface type. We use in this study the BiHemispherical Reflectance (BHR), defined as the radiant exitance divided by irradiance (‘albedo’) under ambient illumination conditions (including both direct and diffuse illumination). This parameter is available in MISR’s four spectral bands. Since MISR retrieval is able to separate the surface from the atmospheric signals, the retrieved BHR will reflect the change in surface optical properties, independent of the aerosols in the atmosphere above. The performance of MISR land surface parameters in classifying vegetation and other surface types has been widely evaluated [e.g., *Hu et al.*, 2007; *Armston et al.*, 2007]. The MISR BHR data has a spatial resolution of $1.1 \times 1.1 \text{ km}^2$, and was also re-sampled to the $17.6 \times 17.6 \text{ km}^2$ grid for analysis.

2.2 Method

Aerosol effect on the TOA albedo ($d\alpha$) in each $2^\circ \times 2^\circ$ latitude-longitude region is defined as the difference between the mean MISR TOA albedo (α) within the region over the time interval of interest (1 month) and the TOA albedo without the presence of aerosols (α_0). Within each $2^\circ \times 2^\circ$ region, there is little variation in the downward solar flux. Thus we simply estimated α from the

arithmetic mean TOA albedo for all data pairs within each $2^\circ \times 2^\circ$ domain. Satellite instruments (including MISR) are not able to observe the aerosol-free TOA albedo directly, since aerosol particles are always present in the atmosphere. To estimate α_0 , we perform linear regressions between the spectral TOA albedo and spectral AOD for all the data pairs that have similar aerosol and surface properties. The y-intercept of each regression line represents the estimated aerosol-free TOA albedo for that region. We also assess the confidence with which this extrapolation can be performed.

In this study, the regression is performed for data pairs in each $2^\circ \times 2^\circ$ region for each month. This selection of spatial and temporal scales preserves enough data samples and AOD dynamic range for the correlation analysis, and simultaneously limits the large variability in aerosol and surface properties, thus maintaining the quality of the linear regressions for most regions. In addition, considering the large variability of surface reflectance over land, we further divide the data pairs in each $2^\circ \times 2^\circ$ region into different sets according to their BHR values. Based on the probability density function of BHR globally (discussed with Figure 3C below), we divide the observed range into 10 evenly distributed sets between 0 and 0.1, and 35 sets between 0.1 and 0.8. We then examine the TOA albedo \sim AOD regression for data sets stratified by BHR within each region. Since the probability distributions of AOD and BHR are spectrally dependent (see Figure 3B and 3C), the linear regression analyses are performed for each spectral band individually.

Figure 1 shows an example of a successful linear regression. The grey points represent all cloud-filtered data pairs associated with AOD and TOA albedo. Since no side contribution is included in the plotted TOA albedo, the correlation is noisy. The inclusion of both the top and side radiance contributions (black points in Figure 1) significantly improves the correlation and reduces the uncertainty in estimating the aerosol-free TOA albedo. The side contribution is

particularly important when a thick aerosol layer (e.g., a smoke or dust plume) is clearly present. The regression line in Figure 1 demonstrates that in the blue band, the presence of these aerosols raises the TOA albedo in this region (for a certain BHR stratum) at a rate of 0.074 per unit of AOD, and the derived aerosol-free TOA albedo is 0.161.

We consider a linear regression successful if the Root Mean Square (RMS) error of the regression is smaller than 0.025, or if the correlation coefficient is larger than 0.5. We also require the number of data pairs in each set be greater than 10, and the AOD dynamic range to be over 0.15. Overall, about 70% of the data pairs in the visible bands produce successful regressions. Several reasons can cause a failure in linear regression. Data points may be too few due to extensive cloud cover or unsuccessful retrievals. Data points may have similar AOD values so that the AOD dynamic range is too small to do the regression. When surface or aerosol properties have large variabilities within a region during a month, a good linear regression between α and AOD is also difficult. The success ratio drops to about 30% for the MISR NIR band. This is likely due to two factors. AODs are typically lower in the NIR than in the visible bands (Ricchiazzi et al., 2006) as a result of smaller aerosol scattering in the former. Additionally, surface reflectivity is higher over some surfaces in the NIR than in the visible bands (Miura et al., 2008).

If the linear regression fails, $d\alpha$ can not be estimated from the difference between α and α_0 , because there is no successful estimate of α_0 for that BHR set within that $2^\circ \times 2^\circ$ region. In such cases, $d\alpha$ is obtained by multiplying the mean AOD for that data set by a scaling factor. The scaling factors were pre-determined from all the available successful regressions globally. For each successful regression, we saved the slope of the AOD- α regression and the mean surface BHR and aerosol SSA of the data used for regression. The regressions were classified into

different groups based on the mean BHR and SSA values, and the mean value of regression slopes for each group was calculated. We fit an empirical expression for the slope (the scaling factor) in terms of BHR and SSA. This empirical scaling factor, which represents the mean ability of aerosols to affect the TOA albedo, was used for estimating $d\alpha$ when local linear regression failed. We prefer this method to simply putting missing data where linear regression fails based on the following considerations. First, we attempted to provide a global average value of $d\alpha$. Since the probability of failure is usually larger over regions with small AODs, the simple average over successful regressions may result in a positively-biased global mean value. Secondly, although the linear regression fails, the information on aerosol and surface properties may still be valid. We tried to utilize this information instead of discarding it.

3. Results

3.1 Global distributions of aerosol and surface properties over land

The TOA albedo change due to the presence of aerosols in cloud-free regions is mainly determined by aerosol loading, aerosol optical properties, and surface reflectance. Figure 2 gives a global view of the four-month (June-September 2007) mean MISR-retrieved AOD, SSA, AE, and surface BHR over land. The AOD, SSA, BHR values are for 0.56 μm (MISR green band). These values are averages for clear-sky only. MISR-retrieved global mean values of AOD, SSA, BHR and AE over land are summarized in Table 2.

High AOD values are seen in desert regions such as the Sahara and the Arabian Peninsula, in polluted regions including South and East Asia, Eastern Europe, Southeast U.S., and in biomass burning regions such as Central Africa and the Amazon (Figure 2a).

271 Aerosol SSA, the ratio of scattering to total light extinction, indicates the relative importance of
272 aerosol scattering versus absorption [*Bergstrom et al.*, 2003]. Figure 2b shows high SSA values
273 (close to unity) in most industrialized and desert regions, where aerosol scattering dominates.
274 Aerosols in biomass burning regions are more absorbing with smaller SSA values. In Central
275 Africa and South America, for example, averaged SSA values are as low as ~ 0.9 , indicating
276 relatively high aerosol absorption. This is also evident in Alaska, Northern Canada and Siberia,
277 where high AODs are correlated with low SSAs (see Figure 2a and 2b).

278 The AE is inversely correlated with the average size of aerosol particles: the smaller the particles,
279 the larger the exponent [*Angstrom*, 1929; *Schuster et al.*, 2006]. Small AE values in desert
280 regions (Figure 2c) are consistent with the presence of large dust particles. Large values of AE
281 are observed over biomass burning and industrial regions where fine-mode aerosols dominate.

282 Previous studies have shown that the fraction of energy reflected at a particular wavelength
283 varies with surface type [e.g., *Kaufman et al.*, 2002b]. The MISR-derived BHR data shown in
284 Figure 2d illustrates that global land surface is very heterogeneous in reflecting solar radiation.
285 The less the vegetation cover, the larger the BHR values usually are in areas with high soil
286 albedo. The largest BHR values are in desert and barren regions. The spectral signatures over
287 different surface types have been observed to be very different [e.g., *Tucker and Sellers*, 1986].
288 For example, the reflectance over sand and soil increases with wavelength in the visible-NIR
289 range, and the rate of increase diminishes at longer wavelengths. Over dense vegetation, the
290 reflectance in the visible region is relatively uniform over the spectrum, with slightly higher
291 values in the green band. From visible bands to NIR, however, there is a large jump in surface
292 reflectance, known as the red-far red edge. These spectral signatures of surface types are well
293 captured by MISR observations (Table 2 and Figure 2d). In vegetated regions, much higher BHR

values are observed in the NIR band than visible bands, whereas in desert and barren areas, the BHR increases smoothly from the blue to the NIR band.

The probability distributions of MISR AOD, SSA, BHR and AE over land are shown in the diagonal panels in Figure 3. Figure 3B shows that AOD has a narrower distribution at longer wavelengths. Most BHR values in visible bands are below 0.2, whereas in the NIR band, a peak near 0.3 is present (Figure 3C). Most SSA distributions are above 0.9, with more small values in blue and green bands (Figure 3D). AE values are mostly distributed between 0.5 and 2, with a broad peak at ~ 1.2 (Figure 3E). The other panels of Figure 3 will be analyzed further in section 3.3.1.

3.2 TOA albedo change by aerosols over land

Based on linear regressions between the MISR TOA albedo and AOD, we estimate the aerosol effect on TOA albedo in the four MISR spectral bands. Figure 4 shows the 4-month (June-September 2007) mean spatial distributions of TOA albedo change due to the presence of aerosols ($d\alpha$) over cloud-free land. Persistent cloud cover over the Amazon, Central Africa, Southeast Asia, and West Canada prevents MISR from observing enough cloud-free data to meet our criteria, so $d\alpha$ values over some portion of these regions are missing.

The global means of $d\alpha$ over cloud-free land are 0.018 (blue), 0.010 (green), 0.007 (red), and 0.008 (NIR). We would expect $d\alpha$ to be large where AOD is high, especially if the aerosols are bright (high SSA) and reside over dark surfaces. We examine first the relationship between $d\alpha$ and AOD and then the relative contributions of surface and aerosol optical properties to $d\alpha$.

The $d\alpha$ patterns show some similarity with the AOD pattern (Figure 2a), i.e., high $d\alpha$ values are found in most high AOD regions, including East Asia, the Indian and Arabian Peninsulas,

316 Western Sahara, East Europe, and North America. However, high AOD is not always
317 accompanied by high $d\alpha$. In some biomass burning regions with relatively small SSA (e.g.,
318 Central Africa, see Figure 2b), $d\alpha$ is small due to aerosol absorption. Small $d\alpha$ is also
319 observed over bright surfaces, such as in northeastern Sahara, and in the desert regions of
320 Australia and Southern Africa.

321 *Patadia et al.* [2008] neglected a large area spanning Northern Africa to middle Asia in their
322 calculation due to inconsistent AOD-flux relations over high reflectance surfaces. The use of
323 internally consistent data sets and BHR stratification in our study produces relatively good
324 correlations between AOD and TOA albedo for this area. The inclusion of these high-reflectance
325 regions, which account for about 10% of Earth's landmass, is necessary to accurately estimate
326 the global aerosol radiative effect. Large aerosol loading (Figure 2a) and intense solar radiation
327 (due to high sun at low latitude and low subtropical cloud cover) have the potential to cause a
328 large aerosol radiative effect in these regions (Figure 4). We estimate that neglecting of these
329 regions would produce an underestimate of global mean $d\alpha$ over land by ~5% of its value.

330 In Figure 4, the detailed patterns of TOA albedo change due to aerosols over the Saharan desert
331 and Arabian Peninsula demonstrate the value of our approach over bright surfaces. The aerosol
332 effect on TOA albedo differs between the western and eastern parts of the highly reflective
333 Saharan desert. In the Western Sahara, aerosol loading is very high (mean AOD is greater than
334 0.5 at 0.56 μ m wavelength, see Figure 2a), and small AE values (Figure 2c) are consistent with
335 the single dominant aerosol component being large dust particles. The $d\alpha$ value in this part is
336 also high (>0.03 at 0.56 μ m). In northeastern Sahara, aerosol loading is much smaller, and the
337 surface reflectance is higher. Relatively higher AE values suggest smaller aerosol size
338 distributions, which could be due to the change in size distribution during dust transport, or

different surface properties producing different mineral dust size distributions. Other sources of aerosols, such as pollution, may also contribute to the presence of small particles. The calculated $d\alpha$ in this region is clearly smaller than that in the western Sahara. Because the surface and dust particles have similar ability to reflect solar radiation, and also because the dust particles are weakly absorbing, negative values of $d\alpha$ (corresponding to a warming effect) are sometimes found in this region. For the southern rim of the Sahara, where a large dust burden occurs over a less reflective surface, $d\alpha$ is largest. There is a similar spatial distribution of $d\alpha$ in the Arabian Peninsula, with large values over darker surfaces in the western part near the Red Sea.

3.3 Dependence of $d\alpha$ and aerosol radiative efficiency on surface reflectance and aerosol optical properties

Latitudinal distributions of spectral $d\alpha$ and MISR AOD at $0.56\mu\text{m}$ are shown in Figure 5a. $d\alpha$ generally decreases from the blue band to red band. The decrease is partly due to the smaller aerosol scattering at longer wavelength, and partly due to increasing surface reflectance from blue to red for most surface types (Table 2), which reduces the contrast between aerosol and the surface. The $d\alpha$ patterns for red band and NIR are similar.

As in Figure 4, the $d\alpha$ distribution generally follows the AOD distribution, with two peaks located in $10\sim 30^\circ\text{N}$ and $0\sim 10^\circ\text{S}$ (see also Figure 2a). However, there are some regions where the $d\alpha$ and AOD distributions do not match one another. For example, $d\alpha$ in the three visible bands decreases from 10°N to 20°N despite the increase in AOD.

In order to interpret these results, we introduce the concept of aerosol radiative efficiency. The aerosol radiative efficiency is defined here as $d\alpha$ normalized with respect to MISR AOD at $0.56\mu\text{m}$. It represents the aerosol's ability to change the TOA albedo. The latitudinal distributions of

spectral aerosol radiative efficiencies, together with the MISR-retrieved surface and aerosol properties (BHR and SSA at 0.56 μm , and AE), are shown in Figure 5b. The aerosol radiative efficiencies have very different latitudinal distributions from the $d\alpha$ distributions but are directly linked to the distributions of aerosol and surface properties. The two dips near 20°N and 30°S are likely due to the large BHR in those regions (also shown in Figure 2d). From 10°N to 20°N, the aerosol radiative efficiency decreases abruptly in the visible bands due to the increase of BHR, which explains why $d\alpha$ decreases despite the increase in AOD (Figure 5a). In other regions where surface reflectance is low, the aerosol radiative efficiency is positively correlated with SSA. From 30°S to 40°S, both the increase of SSA and the decrease of BHR contribute to a significant rise in the aerosol radiative efficiency. The largest efficiency is in the mid-latitude Northern Hemisphere, where the vegetation cover is dense so the surface reflectance is small (see Figure 2d), and the aerosol particles are generally small (see Figures 2c and 5b) and highly scattering (see Figures 2b and 5b).

The patterns shown in Figures 4 and 5 clearly indicate that the TOA albedo change by aerosols, $d\alpha$, is influenced not only by the aerosol radiative properties, but also by surface reflectance. We explore the dependence of $d\alpha$ and aerosol radiative efficiency on surface reflectance and aerosol optical properties in more detail, including AOD, SSA, and AE dependencies.

3.3.1 $d\alpha$

In addition to the probability distribution functions for each variable, discussed above, Figure 3 gives the correlations between calculated $d\alpha$ and MISR AOD, BHR, SSA, and AE. Fitted lines for correlations between each pair of these variables are plotted in panels above the diagonal, based on statistics on all 2°×2° grid cells over land, for June-September 2007.

In general, $d\alpha$ increases, albeit nonlinearly, with increasing AOD (hence larger aerosol scattering) for all four spectral bands (Figure 3a). The slopes are largest in the blue band where the largest aerosol radiative efficiencies occur (see Figure 5b). The slopes tail off at larger AOD values (~ 0.2). This may be partly explained by aerosol multi-scattering at higher aerosol loading [Bissonnette, 1988]. Additionally, brighter surfaces with higher BHR values, where AOD values are typically large (Figure 3e), tend to decrease the aerosol radiative efficiency.

The dependence of $d\alpha$ on surface reflectance is complex. Figure 3b shows that when BHR is small, the correlation between $d\alpha$ and BHR is weak. When BHR is higher, $d\alpha$ starts to increase with increasing BHR. This pattern can be attributed to the correlation between AOD and BHR (Figure 3e), which shows AOD increases with increasing BHR when BHR is large enough. In this regime, the increase in AOD apparently outweighs the decrease of aerosol radiative efficiency caused by increasing BHR (as shown in Figure 5b). When BHR is very large, as shown in Figure 3e, the correlation between AOD and BHR is weak again. In this regime, the increased BHR dominates, leading to decreased aerosol radiative efficiency and smaller slope of $d\alpha \sim \text{BHR}$.

Many studies emphasize the importance of SSA, which represents the relative contributions of aerosol scattering and absorption, in affecting the Earth-atmosphere radiation budget [e.g., Hansen *et al.*, 1998]. Aerosols with large SSA scatter the incoming solar radiation, cooling the atmosphere and surface. For fixed AOD, the net effect of increasing aerosol absorption (lowering SSA) is to decrease TOA albedo, due to the absorption. Figure 3c demonstrates this $d\alpha$ decrease with decreasing SSA, an effect that is more obvious for blue and green bands. For the majority of the SSA range, the change in AOD and BHR with changing SSA is small (Figure 3f and 3h). Therefore, the positive correlation of $d\alpha$ and SSA is mainly caused by the change SSA

makes to the aerosol radiative efficiency. Figure 3c also shows that the spectral difference of $d\alpha$ is largest at high SSA. The spectral difference becomes much smaller when aerosol absorption is important (i.e., SSA is low). This dependence pattern is also seen in Figure 4, which shows the largest $d\alpha$ change from the blue to NIR bands in industrial and desert regions, where SSA is high (Figure 2b). We also notice that when SSA is close to unity, positive correlations between AOD and SSA are present (Figure 3f), which additionally increases the slope of $d\alpha \sim \text{SSA}$ (Figure 3c).

In general, AE is inversely related to the aerosol size. The relationship between $d\alpha$ and AE (Figure 3d) can be explained by the correlations between AE and other aerosol and surface properties (AOD, BHR, and SSA). Over the majority of the AE range (0.5~2.0, as shown in Figure 3E), $d\alpha$ decreases with increasing AE, mainly because of the negative correlation between AOD and AE (Figure 3g). Because BHR also decreases with increasing AE (Figure 3i), the slopes of $d\alpha \sim \text{AE}$ are smaller than those of $\text{AOD} \sim \text{AE}$. Figure 3j shows SSA is also inversely correlated to AE when aerosol size is in the moderate range. Strong light absorption (low SSA) is mainly associated with small particles ($\text{AE} \sim 2$ as shown in Figure 3E). However, small SSA values when $\text{AE} \sim 0$ indicate that very large particles may also absorb light in the blue and green bands. Figure 3j shows that typically, SSA decreases with wavelength for small particles ($\text{AE} > \sim 1.5$), but increases with wavelength for large particles. This is consistent with previous aircraft measurements [Bergstrom *et al.*, 2002]. The different spectral dependence of SSA in the MISR products is a consequence of the particle models underlying the MISR aerosol retrievals and is based on a combination of satellite-measured radiances and prior knowledge from field observations [e.g., Kahn *et al.*, 2001].

Figure 6 demonstrates how the $d\alpha$ dependence on AOD is affected by BHR, SSA and AE (in the green band). The rate of increase of $d\alpha$ with AOD is smaller when BHR is larger. The decreased rate is significant only when AOD is larger than ~ 0.2 . For higher AOD, this difference becomes larger. As might be expected, the $d\alpha \sim$ AOD correlation slope is larger also for brighter (higher SSA) particles. However, the increase in slope is smaller for higher SSA, and is less dramatic than the AOD dependence. Probably due to weak inverse correlation between BHR and AE (Figure 3i), the $d\alpha \sim$ AOD slope is higher when AE is larger.

3.3.2 Aerosol radiative efficiency

To further illustrate the dependence of $d\alpha$ on aerosol properties and surface reflectance, we plot the aerosol radiative efficiency as a function of BHR, SSA, and AE in Figure 7. Because there are not enough data points, lines in Figure 7a stop at certain BHR values. Figure 7a shows that aerosol radiative efficiencies do not change substantially with BHR when the surface is dark (low BHR). When the surface is brighter (i.e., BHR surpasses a critical value), the aerosol radiative efficiencies decrease as BHR increases. This relationship causes a strong correlation between aerosol radiative efficiency and BHR when BHR is large, as shown in Figure 5b. Figure 6a also shows the critical BHR value increases with wavelength, and the slope becomes smaller for longer wavelength.

The positive correlation between aerosol radiative efficiency and SSA (Figure 7b) is similar to that between $d\alpha$ and SSA (Figure 3c). For blue and green bands, the radiative efficiency increases with increasing SSA. This correlation contributes to the agreement between the aerosol radiative efficiency pattern and the SSA pattern (Figure 5b) outside the high BHR region.

The dependence of aerosol radiative efficiency on AE (Figure 7c) can be attributed to the combined effect of the BHR-AE correlation (Figure 3i) and the SSA-AE correlation (Figure 3j). For the blue band, BHR decreases and SSA increases with increasing AE. Both effects contribute to the increase of aerosol radiative efficiency. For the NIR band, the correlation between BHR and AE is weak. The negative correlation between aerosol radiative efficiency and AE is mainly determined by the SSA-AE relationship. For the green and red bands, the two effects nearly cancel out and the aerosol radiative efficiencies are not sensitive to AE.

We should bear in mind that since BHR is predominantly a surface property, the above-mentioned empirical correlation of BHR with aerosol properties may not represent a simple causal relationship. However, some connections are likely, such as bright desert surfaces being the source for bright, and relatively high AOD, airborne mineral dust.

3.3.3 Effect of surface reflectance on aerosol scattering and absorption

As discussed above, the increasing of TOA albedo by aerosol scattering and the decreasing by aerosol absorption together determine the aerosol radiative efficiency. Figure 8 illustrates how the change of surface reflectance mediates the influence of aerosol scattering and absorption. The derived aerosol radiative efficiencies for all $2^\circ \times 2^\circ$ grid cells globally are stratified based on their BHR and SSA values, and the mean aerosol radiative efficiency is shown for each stratum.

Figure 8 helps to additionally separate the contributions from BHR and SSA. When SSA is close to 1 (box 1 within each spectral panel in Figure 8), the dominant effect is aerosol scattering. When the surface is brighter, the net downwelling shortwave radiance passing through the atmosphere is smaller, because the surface reflects more radiance back to the space. In other words, the contrast between the reflectance from aerosols and surface is smaller. This effect decreases the magnitude of TOA albedo change by aerosols. As a consequence, as shown in box

1 of Figure 8, the aerosol radiative efficiencies decrease with increasing BHR for blue, green, and red bands. It is less obvious for for NIR.

When SSA is small, the contribution from absorptive aerosols changes the aerosol radiative efficiency, as well as its dependence on surface reflectance. By using a radiative transfer model, *Satheesh* [2002] showed that for a given aerosol system, the effect of soot absorption is significantly larger over brighter surface (either land or clouds) because the radiation reflected from the surface below would interact with the aerosols again. Our results in Figure 8 (box 2) show such an enhancement as well. As BHR increases, the aerosol radiative efficiency (for constant SSA) decreases, and turns negative when BHR exceeds a certain threshold. The presence of cases with negative values indicates that aerosols may warm the atmosphere when the surface is highly reflective. The amplification effect is especially true for the green and red bands.

3.4 $d\alpha$ patterns over different vegetation types

Vegetation cover determines the ratio of reflection and absorption of solar radiation by the land surface. Knowing the TOA albedo change by aerosols over different vegetation types will help establish how land cover change, such as desertification and deforestation, will alter the aerosol radiative effect. Land cover change may be accompanied by the change of aerosol optical properties, due to the alteration of biogenic emissions, biomass burning, or industrial activities. But on short time scales, we can assume the aerosol optical properties remain unchanged after a change in vegetation type. MODIS provides a 1 km land cover product (MOD12Q1), which includes an IGBP (International Geosphere-Biosphere Programme) land cover classification map of the globe [*Belward et al.*, 1999; *Scepan et al.*, 1999]. We aggregated the MODIS land cover into seven land vegetation types, covering regions where enough land area and sample size are

available - needleleaf forest, broadleaf forest, shrubland, savanna, grassland, cropland, and barren areas. The dominant surface type in each $2^\circ \times 2^\circ$ grid cell was determined and is shown in Figure 9a.

Correlations between blue band $d\alpha$ and AOD over different vegetation types are shown in Figure 9b. Compared to other surface types, barren regions have the lowest slope, indicating aerosols over these regions have the smallest radiative efficiency. Most barren regions are located at $15^\circ \sim 30^\circ \text{N}$ (see Figure 9a), where high surface reflectance (Figure 2d and 5b) reduces the aerosol effect on TOA albedo. However, because the aerosol loading over these regions is generally high (Figure 2a and 5a), the mean $d\alpha$ is still large (See Table 2). Figure 9a shows the southern edge of the Sahara desert to be adjacent to grassland and savanna ecosystems, which have much smaller $d\alpha \sim \text{AOD}$ slope (Figure 9b). Due to this large contrast, the $d\alpha$ in this region has a large gradient (Figure 4b).

Figure 9b also shows the largest dependence of $d\alpha$ on AOD is over croplands, which are mainly located near the industrial regions of the Northern Hemisphere, such as East and South Asia, Europe, and Eastern U.S. (Figure 9a). For a majority of these regions, the SSA value is large (Figure 2b) and BHR is small (Figure 2d), which both contribute to large aerosol radiative efficiency ($30^\circ \sim 60^\circ \text{N}$ in Figure 5b). In addition, these regions have moderate to large AOD (Figure 2a), likely due to anthropogenic emissions. All these factors make croplands the vegetation type with largest $d\alpha$ (Table 2).

Over most forests and grasslands, the correlations between $d\alpha$ and AOD are similar (Figure 9b), which means the aerosol radiative efficiency would be similar given similar AOD distributions. However, because aerosol loading over needleleaf and shrublands is small (Table 2), the aerosol radiative efficiency and $d\alpha$ in these regions are small.

The mean values of $d\alpha$ over different land vegetation types in all four MISR spectral bands are summarized in Table 2. A decrease of $d\alpha$ from short wavelength (blue band) to long wavelength (NIR) is seen for most vegetation types. Overall, the smallest $d\alpha$ values are over needleleaf forests and shrublands, whereas the largest values are over cropland and barren regions. The aerosol radiative efficiencies are lowest over needleleaf forest and barren regions, and highest over grasslands and croplands.

4. Uncertainty

In this study, we use the MISR TOA albedo product and aerosol properties to derive the aerosol effect on TOA albedo. The availability of good quality AOD makes it possible to derive aerosol radiative effect over bright land surfaces. We also use MISR BHR to stratify the surface, which decouples the effects contributed by aerosols and surface. Despite these improvements, both unbiased and biased uncertainties still exist in the current estimation of TOA albedo change by aerosols. In this study, we consider three types of uncertainties: the uncertainty from the linear regressions, the uncertainty from the intrinsic scatter of MISR retrieved data, and the uncertainty due to cloud contamination.

In the present study, the y-intercept of the TOA albedo \sim AOD linear regression is assumed to be the aerosol-free TOA albedo. *Isobe et al.* [1990, Equation 9] provide an approach for calculating the variance of the intercept from a linear regression. Based on this approach, we estimate the variance of $d\alpha$ for each linear regression. When the regression is not successful, $d\alpha$ is estimated from the mean AOD and a pre-determined scaling factor that depends on the mean SSA and BHR values for the region, as described in Section 2.2. Since the derivation of this scaling factor is based on the slopes (b) of all available successful regressions, we simply assume the variance

541 of the scaling factor is twice the mean variances of slopes. The variance of the slope (b) for each
 542 successful regression is also derived using the method of *Isobe et al.* [1990]. For each $2^\circ \times 2^\circ$ grid
 543 cell, the mean variance of $d\alpha$ is the sample-number-weighted mean variance of $d\alpha$ for every
 544 BHR set, including successful and unsuccessful regressions. By assuming the variance of $d\alpha$ is
 545 uncorrelated over different regions, we estimate the overall error due to the linear regression
 546 derived from this study is 0.0013 (blue), 0.0012 (green), 0.0015 (red), and 0.0019 (NIR).

547 The uncertainty of $d\alpha$ also results from the intrinsic uncertainty of MISR retrieved AOD and
 548 TOA albedo. By comparing a 2-year measurement record of globally distributed AERONET Sun
 549 photometers, *Kahn et al.* [2005] showed that about 1σ of the MISR-retrieved AOD values fall
 550 within ± 0.05 (or 20%) of AERONET. Here we use 20% as the uncertainty range of global mean
 551 AOD in all four bands. By multiplying this uncertainty by the mean slope of the TOA albedo-
 552 AOD relationship (~ 0.04 per unit of AOD), we obtain an additional uncertainty of 0.002 in the
 553 global mean $d\alpha$. The radiometric uncertainty of MISR radiances due the calibration is about 3-
 554 4% [*Bruegge et al.*, 2007]. In the MISR retrieval, top-leaving radiances were integrated either
 555 using an azimuthal model (AZM) or a Solid Angle Weighting method for cloud-free scenes.
 556 There are uncertainties in determining the integration coefficients for either method [*Diner et al.*,
 557 1999]. The standard deviation of the albedo values with the AZM approach has been evaluated
 558 for different surface types in cloud-free scenes. Most albedo errors lie between 1% and 2%
 559 [*Diner et al.*, 1999; *Sun et al.*, 2006]. So we estimate the uncertainty of $d\alpha$ caused by the
 560 intrinsic uncertainty in MISR retrieved TOA albedo to be $4\% \times \overline{d\alpha}$, where $\overline{d\alpha}$ is the global
 561 mean of the TOA albedo change by aerosols. We estimate global mean of this uncertainty to be
 562 0.00072 (blue), 0.0004 (green), 0.00028 (red), 0.00032 (NIR).

Another source of uncertainty results from the use of a cloud mask to distinguish the cloudy from the cloud-free regions. Although we use stringent cloud screening in this study to minimize the cloud effect (see section 2.1), occasional misclassification of cloudy region as cloud-free region will systematically introduce a high bias. Additionally, the neglect of partly cloud-covered regions may bias the results toward situations dominated by large high-pressure systems [Remer and Kaufman, 2006]. However, this source of uncertainty is difficult to quantify, due to the scarcity of relevant studies. To estimate this uncertainty, we used two independent cloud mask products derived from MISR observations (SVM Cloud Confidence Level and the Cloudy Clear Designator). We also tried looser and more stringent ways of aggregating the cloud masks to $17.6 \times 17.6 \text{ km}^2$ resolution. We find that the global mean $d\alpha$ varies by 0.0015 (blue), 0.0012 (green), 0.0020 (red), 0.0051 (NIR) due to the use of different cloud masks.

If we assume the uncertainties from different sources are uncorrelated, the total variance is the sum of variances from all the above-mentioned sources. Based on this calculation, the total uncertainty of global mean $d\alpha$ in this study is estimated to be 0.0029 (blue), 0.0027 (green), 0.0032 (red), 0.0058 (NIR). By neglecting the diurnal and seasonal cycle, this corresponds to an uncertainty in clear-sky aerosol SWDRE of $\sim 1.2 \text{ W/m}^2$.

However, regional uncertainties could be higher, and additional bias errors may exist. For example, in regions with large spatial variability of aerosol and surface properties, the correlations between TOA albedo and AOD are generally small and the $d\alpha$ uncertainty is high. Over desert regions where surface reflectance is high, the aerosol retrievals may contain some information from the surface, causing an overestimation of the aerosol radiative effect. The lack of small AOD values (particularly in the NIR band) may bring on additional uncertainty to the linear regression (small perturbation at high AOD may cause large variation in retrieved

intercept). The regressions could also deteriorate when persistent cloud cover is present so that the total number of data samples is small. It should also be noted that uncertainties contributed by the regional correlations are not included in the present analysis.

5. Summary and Conclusions

Despite recent major advances in atmospheric modeling and measurements, there is still large uncertainty in the estimation of the global aerosol radiative effect. Particularly, due to the difficulty of retrieving AOD over bright land surfaces, satellite based estimation of aerosol radiative effect over such surfaces is still missing [Yu *et al.*, 2006]. Another major challenge is due to the highly heterogeneous nature of land surface types. The study presented in this paper demonstrates how internally consistent MISR aerosol, albedo, and surface observations can be used to assess the aerosol effect on TOA albedo over global land. More importantly, by using more reliable MISR AOD and aerosol properties over bright land surfaces, and BHR stratification to decouple aerosol and surface effects, this approach not only expands the spatial coverage, but also reduces the uncertainty in aerosol radiative effect estimates on global land.

We have estimated the four-month (June-September 2007) mean value of clear-sky TOA albedo change due to the presence of aerosols ($d\alpha$) over global land to be 0.018 ± 0.003 (blue), 0.010 ± 0.003 (green), 0.007 ± 0.003 (red), and 0.008 ± 0.006 (NIR). Major uncertainties originate from the linear regressions, the intrinsic scatter of MISR retrieved data, and cloud contamination. Individual regions show large spatial variability. Largest values of $d\alpha$ occur in the latitude bands $10^\circ \sim 30^\circ \text{N}$ and $0^\circ \sim 10^\circ \text{S}$. The mean $d\alpha$ at $0.56 \mu\text{m}$ over bright Saharan Desert and Arabian Peninsula is 0.015. Neglecting these areas would cause an underestimation of the mean value over global land by $\sim 5\%$.

609 The global patterns of $d\alpha$ are determined mainly by aerosol loading and surface reflectivity
610 (BHR); aerosol radiative efficiency (defined as $d\alpha$ normalized by AOD at $0.56\mu\text{m}$) helps isolate
611 the AOD contributions from other factors. In general, $d\alpha$ increases with increasing AOD, with
612 increasing SSA, and with decreasing surface brightness, as expected. But the dependence of $d\alpha$
613 on AOD decreases at high AOD, possibly due to a positive correlation between AOD and BHR.
614 The slopes of $d\alpha$ also decrease with increasing particle size (i.e., with decreasing AE); the AE
615 dependence is apparently due to its negative correlation with AOD.

616 Aerosol radiative efficiency is influenced by the surface reflectance and SSA. When SSA is high,
617 the dominant aerosol scattering effect increases the TOA albedo. Over bright (high BHR)
618 surfaces, the added contribution of aerosol scattering is less significant, which diminishes the
619 aerosol radiative efficiency. When SSA is small and aerosol absorption is important, the TOA
620 albedo change due to the presence of aerosols is also small, because absorbing aerosols reduce
621 the radiance scattered back to space. This effect is enhanced over bright surfaces. In regions with
622 high BHR and low SSA, the aerosol radiative efficiency can be negative, i.e., aerosols may exert
623 a warming effect on the atmosphere. The four-month mean aerosol radiative efficiencies over
624 global land derived from this study are 0.089 (blue), 0.050 (green), 0.035 (red), 0.040 (NIR).

625 We also divided the global land surface into seven vegetation cover types and calculated the
626 mean $d\alpha$ for each type. Despite the large surface reflectance, $d\alpha$ over barren regions is high
627 due to the large aerosol loading. The $d\alpha$ over global croplands is also high, attributed to the
628 small BHR and large SSA. Smallest $d\alpha$ is over needleleaf forests and shrublands, where the
629 aerosol loading is small.

630 Aerosols affect the radiative balance in the atmosphere by modifying the TOA albedo. The $d\alpha$
631 calculated in this study is a first step toward to estimating aerosol broadband shortwave direct

radiative effect (SWDRE). First, the change of spectral TOA albedo due to the presence of aerosols can be converted to the change of TOA broadband radiative flux. Second, since the Terra satellite which carries the MISR instrument is in a sun-synchronous orbit, the current estimated $d\alpha$ is only an ‘instantaneous’ value and a daily cycle albedo model must be applied to convert this value to daily mean value. A multi-spectral radiation transfer model will facilitate these conversions [e.g., *Kaufman et al.*, 2002b].

The method presented in this paper can be extended to over ocean with some modifications. MISR BHR product is not available over ocean. Solar zenith angle, wind speed and ocean chlorophyll concentration are major factors affecting the ocean surface albedo (*Jin et al.*, 2004). We can use these parameters to stratify the ocean surface and do similar regressions in each stratum. The detailed estimation of aerosol SWDRE over global land and ocean using MISR observations will be addressed in Part II of this series. Additionally, direct aerosol forcing has to be extended into partly cloudy and cloudy regions. These regions are likely to have high TOA reflectances, and consequently small or negative values of $d\alpha$. Including these areas will decrease the aerosol SWDRE.

The aerosol radiative effect estimated in this study includes contributions from both natural and anthropogenic aerosols. In addition to the composite aerosol amount and optical properties, MISR is also able to provide the aerosol optical depth stratified by aerosol types [*Kahn et al.*, 2001; *Kalashnikova and Kahn*, 2006; *Chen et al.*, 2008]. This aerosol climatology information, which will be recorded in a future MISR Level 3 Joint Aerosol Research Product, can be exploited to distinguish natural aerosol effect from anthropogenic influences. Following a similar approach as we used here, these data will make possible improved estimation of aerosol radiative forcing over land.

655

656

657 **Acknowledgments**

658 This work is performed at the Jet Propulsion Laboratory, California Institute of Technology,
659 under contract with NASA. The research of Y. Chen is funded in part by the NASA Earth
660 Observing System MISR project, and in part by NASA grant # 622-59-66-40. Q. Li is supported
661 in part by the NASA Atmospheric Composition Modeling and Analysis program. The work of R.
662 Kahn is funded in part by the NASA Earth Sciences Climate & Radiation and Atmospheric
663 Composition programs, under H. Maring and P. DeCola, respectively, and in part by the MISR
664 project. MISR data were obtained from the NASA Langley Atmospheric Sciences Data Center
665 (<http://www.eosweb.larc.nasa.gov>).

666

667

668 **References**

669 Abdou, W. A., D. J. Diner, J. V. Martonchik, C. J. Bruegge, R. A. Kahn, B. J. Gaitley, K. A.

670 Crean, L. A. Remer, and B. Holben (2005), Comparison of coincident MISR and MODIS aerosol

671 optical depths over land and ocean scenes containing AERONET sites, *J. Geophys. Res.*, 110,

672 D10S07, doi:10.1029/2004JD004693.

673 Anderson, T. L., R. J. Charlson, N. Bellouin, O. Boucher, M. Chin, S. A. Christopher, J.

674 Haywood, Y. J. Kaufman, S. Kinne, J. A., Ogren, L. A. Remer, T. Takemura, D. Tanre, O.

675 Torres, C. R. Trepte, B. A. Wielicki, D. M. Winker, and H. Yu (2005), An “A-Train” strategy for

676 quantifying direct climate forcing by anthropogenic aerosols, *Bull. Amer. Meteor. Soc.*, 86, 1785-

677 1809.

678 Angstrom, A. (1929), On the atmospheric transmission of Sun radiation and on dust in the air,

679 *Geogr. Ann.*, 11, 156– 166.

680 Armston, J. D., P. F. Scarth, S. R. Phinna, and T. J. Danaher (2007), Analysis of multi-date

681 MISR measurements for forest and woodland communities, Queensland, Australia, *Rem. Sens.*

682 *Environ.*, 107, 287-298.

683 Belward, A. S., J. E. Estes, and K. D. Kline (1999), The IGBP-DIS Global 1-km Land-Cover

684 Data Set DISCover: A Project Overview, *Photogrammetric Engineering & Remote Sensing*,

685 1999/9: 1013-1020.

686 Bergstrom, R. W., P. B. Russell, and P. Hignett (2002), Wavelength Dependence of the

687 Absorption of Black Carbon Particles: Predictions and Results from the TARFOX Experiment

688 and Implications for the Aerosol Single Scattering Albedo, *J. Atmos. Sci.*, 59, 3, 567-777.

689 Bergstrom, R. W., P. Pilewskie, B. Schmid, and P. B. Russell (2003), Estimates of the spectral
 690 aerosol single scattering albedo and aerosol radiative effects during SAFARI 2000, *J. Geophys.*
 691 *Res.*, 108, D13, doi: 10.1029/2002JD002435.

692 Betts, A. K., J. H. Ball, A. C. M. Beljaars, M. J. Miller, and P. A. Viterbo (1996), The land
 693 surface-atmosphere interaction: A review based on observational and global modeling
 694 perspectives, *J. Geophys. Res.*, 101(D3), 7209–7225.

695 Bissonnette, L. R. (1988), Multiscattering model for propagation of narrow light beams in
 696 aerosol media, *Applied Optics*, 27, 12, 2478-2484.

697 Bruegge, C. J., D. J. Diner, R. A. Kahn, N. Chrien, M. C. Helmlinger, B. J. Gaitley, and W. A.
 698 Abdou (2007), The MISR radiometric calibration process, *Rem. Sens. Environ.* 107, 2-11.

699 Charlson, R. J., J. Langner, and H. Rodhe (1990), Sulphate aerosol and climate, *Nature*, 348, 22.

700 Chen, W-T., R. Kahn, W-H. Li, and J. Seinfeld (2008), Sensitivity of multiangle imaging to
 701 optical and microphysical properties of biomass burning aerosols, *J. Geophys. Res.*, 113, D10203,
 702 doi:10.1029/2007JD009414.

703 Christopher, S. A., J. Chou, J. Zhang, X. Li, T. A. Berendes and R. M. Welch (2000), Shortwave
 704 direct radiative forcing of biomass burning aerosols estimated using VIRS and CERES data,
 705 *Geophys. Res. Lett.*, 27, 2197-2200.

706 Christopher, S. A., and J. Zhang (2002), Shortwave aerosol radiative forcing from MODIS and
 707 CERES observations over the oceans, *Geophys. Res. Lett.*, 29, 1859, doi:
 708 10.1029/2002GL014803.

709 Chu, D., Y. Kaufman, C. Ichoku, L. Remer, D. Tanre, and B. Holben (2002), Validation of
 710 MODIS aerosol optical depth retrieval over land, *Geophys. Res. Lett.*, 29, 1617,
 711 doi:10.1029/2002GL013205.

712 Chylek, P., and J. A., Coakley, Jr. (1974), Aerosols and climate, *Science*, 183, 75-77.

713 Chylek, P., U. Lohmann, M. Dubey, M. Mishchenko, R. Kahn, and A. Ohmura (2007), Limits on
 714 climate sensitivity derived from recent satellite and surface observations, *J. Geophys. Res.*, 112,
 715 D24S04, doi: 10.1029/2007JD008740.

716 Coakley Jr., J. A., R. D. Cess, and F. B. Yurevich (1983), The effect of tropospheric aerosols on
 717 the earth's radiation budget: A parameterization for climate models, *J. Atmos. Sci.*, 40, 116-138.

718 Diner, D. J., J. C. Beckert, T. H. Reilly, C. J. Bruegge, J. E. Conel, R. Kahn, J. V. Martonchik, T.
 719 P. Ackerman, R. Davies, S. A. W. Gerstl, H. R. Gordon, J-P. Muller, R. Myneni, R. J. Sellers, B.
 720 Pinty, and M. M. Verstraete (1998), Multi-angle Imaging SpectroRadiometer (MISR) description
 721 and experiment overview, *IEEE Trans. Geosci. Rem. Sens.*, 36 (4), 1072-1087.

722 Diner, D. J., R. Davies, T. Varnai, C. Moroney, C. Borel, S. A. W. Gerstl, and D. L. Nelson
 723 (1999), MISR level 2 top-of-atmosphere albedo algorithm theoretical basis, Rep. D13401, Rev.
 724 D, Jet. Propul. Lab., Pasadena, California. Available at
 725 http://eosps0.gsfc.nasa.gov/eos_homepage/for_scientists/atbd/docs/MISR/atbd-misr-08.pdf.

726 Diner, D. J., W. A. Abdou, T. P. Ackerman, K. Crean, H.R. Gordon, R. A. Kahn, J. V.
 727 Martonchik, S. McMuldroy, S. R. Paradise, B. Pinty, M. M. Verstraete, M. Wang, and R. A.
 728 West (2001), MISR level 2 aerosol retrieval algorithm theoretical basis, Rep. D11400, Rev. E,
 729 Jet. Propul. Lab., Pasadena, California. Available at
 730 http://eosps0.gsfc.nasa.gov/eos_homepage/for_scientists/atbd/docs/MISR/atbd-misr-09.pdf.

731 Diner D. J., B. H. Braswell, R. Davies, N. Gobron, J. Hu, Y. Jin, R. A. Kahn, Y. Knyazikhin, N.
 732 Loeb, J.-P. Muller, A. W. Nolin, B. Pinty, C. B. Schaaf, G. Seiz and J. Stroeve (2005), The value
 733 of multiangle measurements for retrieving structurally and radiatively consistent properties of
 734 clouds, aerosols, and surfaces, *Remote Sensing of Environment*, 97, 495-518.

735 Hansen, J., M. Sato, A. Lacis, R. Ruedy, I. Tegen, and E. Matthews (1998), Climate forcings in
 736 the Industrial era, *Proc. Natl. Acad. Sci.*, 95, 12,753-12,758

737 Hu, J., Y. Su, B. Tan, D. Huang, W. Yang, M. Schull, M. A. Bull, J. V. Martonchik, D. J. Diner,
 738 and Y. Knyazikhin (2007), Analysis of the MISR LAI/FPAR product for spatial and temporal
 739 coverage, accuracy and consistency, *Rem. Sens. Environ.*, 107, 334-347.

740 IPCC (Intergovernmental Panel on Climate Change) (2007), IPCC Fourth Assessment Report:
 741 Climate change 2007, Cambridge University Press, Cambridge.

742 Isobe, T., E. D. Feigelson, M. G. Akritas, and G. J. Babu (1990), Linear regression in astronomy,
 743 *The Astrophysical Journal, part I*, 364: 104-113.

744 Jin, Z., T. P. Charlock, W. L. Smith Jr., and K. Rutledge (2004), A parameterization of ocean
 745 surface albedo, *Geophys. Res. Lett.*, 31, L22301, doi:10.1029/2004GL021180.

746 Kahn, R., P. Banerjee, and D. McDonald (2001), The Sensitivity of Multiangle Imaging to
 747 Natural Mixtures of Aerosols Over Ocean, *J. Geophys. Res.*, 106, 18219-18238.

748 Kahn, R., B. Gaitley, J. Martonchik, D. Diner, K. Crean, and B. Holben (2005), MISR global
 749 aerosol optical depth validation based on two years of coincident AERONET observations, *J.*
 750 *Geophys. Res.*, 110, D10S04, doi:10.1029/2004JD004706.

751 Kalashnikova, O. V. and R. A. Kahn (2006), The ability of multi-angle remote sensing
 752 observations to identify and distinguish mineral dust types: Part 2, Sensitivity data analysis, *J.*
 753 *Geophys. Res.*, 111, D11207, doi:10.1029/2005JD006756.

754 Kaufman, Y., D. Tanre, and O. Boucher (2002a), A satellite view of aerosols in the climate
 755 system, *Nature*, 419, 215-223.

756 Kaufman, Y. J., N. Gobron, B. Pinty, J.-L. Widlowski, and M. M. Verstraete (2002b),
 757 Relationship between surface reflectance in the visible and mid-IR used in MODIS aerosol
 758 algorithm – theory, *Geophys. Res. Lett.*, 23, 2116, doi: 10.1029/2001GL014492.

759 Kinne, S., M. Schulz, C. Textor, S. Guibert, Y. Balkanski, S. E. Bauer, T. Berntsen, T. F.
 760 Berglen, O. Boucher, M. Chin, W. Collins, F. Dentener, T. Diehl, R. Easter, J. Feichter, D.
 761 Fillmore, S. Ghan, P. Ginoux, S. Gong, A. Grini, J. Hendricks, M. Herzog, L. Horowitz, I.
 762 Isaksen, T. Iversen, A. Kirkevag, S. Kloster, D. Koch, J. E. Kristjansson, M. Krol, A. Lauer, J. F.
 763 Lamarque, G. Lesins, X. Liu, U. Lohmann, V. Montanaro, G. Myhre, J. Penner, G. Pitari, S.
 764 reddy, O. Seland, P. Stier, T. Takemura, and X. Tie (2006), An AeroCom initial assessment –
 765 optical properties in aerosol component modules of global models, *Atmos. Chem. Phys.*, 6, 1815-
 766 1834.

767 Liu, Y., J. Sarnat, B. Coull, P. Koutrakis, and D. J. Jacob (2004), Validation of Multi-angle
 768 Spectroradiometer (MISR) aerosol optical thickness measurements using Aerosol robotic
 769 Network (AERONET) observations over the contiguous United States, *J. Geophys. Res.*, 109,
 770 D06025, doi:10.1029/2003JD003981.

771 Loeb, N. G., and S. Kato (2002), Top-of-atmosphere direct radiative effect of aerosols over the
 772 tropical oceans from the Clouds and the Earth's Radiant Energy System (CERES) satellite
 773 instrument, *J. Climate*, 15, 1474-1484.

774 Loeb, N. G., and N. Manalo-Smith (2005), Top-of-atmosphere direct radiative effect of aerosols
 775 over global oceans from merged CERES and MODIS observations, *J. Climate*, 18, 3506-3526.

776 Martonchik, J. V., D. J. Diner, R. Kahn, and B. Gaitley (2004), Comparison of MISR and
 777 AERONET aerosol optical depths over desert sites, *Geophys. Res. Lett.*, 31, L16102, doi:
 778 10.1029/2004GL019807.

779 Mazzoni, D., M. Garay, R. Davies, and D. Nelson (2007), An operational MISR pixel classifier
 780 using Support Vector Machines, *Rem. Sens. Env.* 107, 149-158.

781 Mishchenko, M. I., I. V. Geogdzhayev, W. B. Rossow, B. Cairns, B. E. Carlson, A. A. Lacis, L.
 782 Liu, L. D. Travis (2007), Long-Term Satellite Record Reveals, *Science*, 315, 1543.

783 Miura, T., H. Yoshioka, K. Fujiwara, and H. Yamamoto (2008), Inter-Comparison of ASTER
 784 and MODIS surface reflectance and vegetation index products for synergistic applications to
 785 natural resource monitoring, *Sensors*, 8, 2480-2499.

786 NASA/University of Maryland (2002), MODIS Hotspot / Active Fire Detections. Data set.
 787 MODIS Rapid Response Project, NASA/GSFC [producer], University of Maryland, Fire
 788 Information for Resource Management System [distributors]. Available on-line at
 789 <http://maps.geog.umd.edu>.

790 Patadia, F., P. Gupta, and S. A. Christopher (2008), First observational estimates of global clear
 791 sky shortwave aerosol direct radiative effect over land, *Geophys. Res. Lett.*, 35, L04810, doi:
 792 10.1029/2007GL032314.

793 Quinn, P. K., T. S. Bates, D. J. Coffman, T. L. Miller, J. E. Johnson, D. S. Covert, J. P. Putaud, C.
 794 Neususs, and T. Novakov (2000), A comparison of aerosol chemical and optical properties from
 795 the 1st and 2nd Aerosol Characterization Experiments, *Tellus B*, 52, 239-257.

796 Quinn, P. K., and T. S. Bates (2005), Regional aerosol properties: comparisons of boundary layer
 797 measurements from ACE 1, ACE 2, aerosol99, INDOEX, ACE asia, TARFOX, and NEAQS, *J.*
 798 *Geophys. Res.*, 110, D14202, doi: 10.1029/2004JD004755.

799 Remer, L. A. and Y. J. Kaufman (2006), Aerosol direct radiative effect at the top of the
 800 atmosphere over cloud free ocean derived from five years of MODIS data, *Atmos. Chem. Phys.*,
 801 6, 237–253.

802 Ricchiazzi, P., C. Gautier, J. A. Ogren, and B. Schmid (2006), A comparison of aerosol optical
 803 properties obtained from in situ measurements and retrieved from Sun and sky radiance
 804 observations during the May 2003 ARM Aerosol Intensive Observation Period, *J. Geophys. Res.*,
 805 111, D05S06, doi: 10.1029/2005JD005863.

806 Satheesh, S. K. (2002), Aerosol radiative forcing over land: effect of surface and cloud reflection,
 807 *Annales Geophysicae*, 20: 2105-2109.

808 Scepan, J., G. Menz and M. C. Hansen (1999), The DISCover Validation Image Interpretation
 809 Process, *Photogrammetric Engineering & Remote Sensing*, 1999/9: 1075-1081.

810 Schuster, G. L., O. Dubovik, and B. N. Holben (2006), Angstrom exponent and bimodal aerosol
 811 size distributions, *J. Geophys. Res.*, 111, doi: 10.1029/2005JD006328.

812 Sun, W., N. G. Loeb, R. Davies, K. Loukachine, and W. F. Miller (2006), Comparison of MISR
 813 and CERES top-of-atmosphere albedo, *Geophys. Res. Lett.*, 33, L23810, doi:
 814 10.1029/2006GL027958.

815 Tucker, C. J. and P. J. Sellers (1986), Satellite remote sensing of primary productivity, *Int. J.*
816 *Remote Sensing*, 7:1395-1416.

817 Yu, H., R. E. Dickinson, M. Chin, Y. J. Kaufman, M. Zhou, Y. Tian, O. Dubovik, and B. N.
818 Holben (2004), The direct radiative effect of aerosols as determined from a combination of
819 MODIS retrievals and GOCART simulations, *J. Geophys. Res.*, 109, D03206,
820 doi:10.1029/2003JD003914.

821 Yu, H., Y. J. Kaufman, M. Chin, G. Feingold, L. A. Remer, T. L. Anderson, Y. Balkanski, N.
822 Bellouin, O. Boucher, S. Christopher, P. DeCola, R. Kahn, D. Koch, N. Loeb, M. S. reddy, M.
823 Schulz, T. Takemura, and M. Zhou (2006), A review of measurement-based assessments of the
824 aerosol direct radiative effect and forcing, *Atmos. Chem. Phys.*, 6, 613-666.

825

826

827

Figure captions

Figure 1. An example of linear regression used for estimating aerosol-free TOA albedo ($\sim 60^\circ\text{N}$, 94°W ; $0.04 < \text{BHR} < 0.05$). Each black dot represents a data pair with spectral (blue band in this case) AOD and TOA albedo (with side contribution). The y-intercept of the regression line (dashed) represents the derived spectral TOA albedo in the absence of aerosols. Grey dots show the data pairs with AOD and TOA albedo from MISR standard product when the side contributions of radiance associated with each RLRA column are not included.

Figure 2. Global over-land distribution of MISR-observed (a) AOD, (b) SSA, (c) AE, and (d) surface BHR in cloud-free land region, averaged over June-September 2007, at $2^\circ \times 2^\circ$ spatial resolution. The AOD, SSA, and BHR values shown are for the MISR green band ($0.56\mu\text{m}$).

Figure 3. Probability distributions of $d\alpha$, AOD, BHR, SSA, and AE over global land are shown in diagonal panels (A ~ E). Also shown are fitted lines on the pairwise scatter plots of these variables (a ~ j). All plots are based on mean values of these variables in $2^\circ \times 2^\circ$ regions during June-September 2007. Colored lines correspond to the four spectral bands (purple for NIR).

Figure 4. Global distribution of TOA albedo change by aerosols ($d\alpha$) in the four MISR bands (a: blue; b: green; c: red; d: NIR) over cloud-free land regions, averaged over June-September 2007, at $2^\circ \times 2^\circ$ spatial resolution.

Figure 5. Latitudinal distributions of (a) $d\alpha$ and (b) aerosol radiative efficiency in four spectral bands: blue (blue line), green (green line), red (red line), and NIR (purple line). The distribution of MISR AOD ($0.56\mu\text{m}$) (black dashed line in (a)) and BHR ($0.56\mu\text{m}$), SSA ($0.56\mu\text{m}$), and AE (black lines in (b)) are also shown. These data are averaged over June-September 2007.

Figure 6. (a) Dependence of $d\alpha \sim \text{AOD}$ correlations on BHR in the green band. Grey line is the fitted line on correlation between $d\alpha$ and AOD for data sets with small BHR (smaller than the median of all BHR values in $2^\circ \times 2^\circ$ regions globally). Black line represents the correlation for data sets with large BHR (larger than median). Green line is fitted line for the whole data set. (b) Similar to (a), except for small and large SSA. (c) Similar to (a), except for small and large AE.

Figure 7. Aerosol radiative efficiency versus BHR, SSA, and AE in four spectral bands.

Figure 8. Aerosol radiative efficiencies versus BHR and SSA in four spectral bands. red color means that the aerosols increase the TOA albedo, while the blue color indicates the aerosol effect on TOA albedo is negative. Box 1 and box 2 represent cases with high SSA and low SSA, respectively.

Figure 9. (a) Global map of aggregated vegetation types derived from annual mean MODIS land cover product. (b) Calculated $d\alpha$ versus AOD in the green band ($0.56\mu\text{m}$) over different vegetation types. The black line shows the globally averaged values over all vegetation types.

Table 1: Summary of MISR products and parameters used in this study

| Product | Parameter | Version | Spatial Resolution (km×km) | Explanation |
|---------------|---------------------------------|----------|----------------------------|--|
| TC_Albedo | AlbedoLocal ¹ | F05_0011 | 2.2×2.2 | TOA local albedo, derived from top-leaving Bidirectional Reflectance Factors (BRFs) only |
| | BRFSide_Mean | | 2.2×2.2 | Mean value of BRFs registered to the side of a column |
| | NumUnobscureSide | | 2.2×2.2 | Number of unobscured pixels with BRFs registered to the side of a column |
| | CloudyClearDesignation | | 2.2×2.2 | Cloudy-Clear designation determined from SCCM and ASCM |
| TC_Classifier | SVMCloudConfidenceLevel | F05_0010 | 1.1×1.1 | Support Vector Machine (SVM) derived cloud confidence level |
| AS_Land | LandBHR | F06_0021 | 1.1×1.1 | Bi-Hemispheric Reflectance over land |
| AS_Aerosol | RegBestEstimateSpectralOptDepth | F11_0021 | 17.6×17.6 | Best estimated aerosol optical depth |
| | RegBestEstimateSpectralSSA | | 17.6×17.6 | Best estimated aerosol single scattering albedo |
| | RegBestEstimateAngstromExponent | | 17.6×17.6 | Best estimated aerosol angstrom exponent |

¹ AlbedoLocal, BRFSide_Mean, NumUnobscureSide, LandBHR, RegBestEstimateSpectralOptDepth, and RegBestEstimateSpectralSSA are available for four spectral bands

Table 2: Mean values of MISR spectral AOD, SSA, AE, BHR, and derived $d\alpha$ and aerosol radiative efficiency over global land and over each vegetation type for June-September 2007. The values are given for MISR blue (B), green (G), red (R), and near infrared (N) bands. Uncertainties are provided when available¹.

| Parameters | | Global land | Needle leaf forest | Broad leaf forest | Shrub land | Savanna | Grass land | Crop land | Barren |
|------------------------------|---|--------------------|--------------------|-------------------|------------|---------|------------|-----------|--------|
| AOD | B | 0.256±0.051 | 0.124 | 0.241 | 0.176 | 0.248 | 0.225 | 0.271 | 0.404 |
| | G | 0.202±0.040 | 0.091 | 0.184 | 0.135 | 0.182 | 0.174 | 0.204 | 0.343 |
| | R | 0.167±0.033 | 0.070 | 0.148 | 0.120 | 0.140 | 0.143 | 0.161 | 0.303 |
| | N | 0.132±0.026 | 0.051 | 0.112 | 0.085 | 0.101 | 0.113 | 0.120 | 0.261 |
| SSA | B | 0.964 | 0.964 | 0.953 | 0.963 | 0.955 | 0.974 | 0.972 | 0.974 |
| | G | 0.971 | 0.966 | 0.963 | 0.968 | 0.958 | 0.981 | 0.976 | 0.984 |
| | R | 0.974 | 0.967 | 0.968 | 0.971 | 0.958 | 0.984 | 0.978 | 0.989 |
| | N | 0.973 | 0.964 | 0.965 | 0.971 | 0.955 | 0.985 | 0.977 | 0.990 |
| AE | | 1.170 | 1.413 | 1.222 | 1.228 | 1.373 | 1.115 | 1.356 | 0.845 |
| BHR | B | 0.067 | 0.043 | 0.054 | 0.067 | 0.051 | 0.068 | 0.054 | 0.114 |
| | G | 0.103 | 0.063 | 0.057 | 0.105 | 0.077 | 0.117 | 0.086 | 0.202 |
| | R | 0.120 | 0.044 | 0.041 | 0.122 | 0.082 | 0.139 | 0.079 | 0.285 |
| | N | 0.246 | 0.215 | 0.185 | 0.245 | 0.239 | 0.272 | 0.286 | 0.340 |
| $d\alpha$ | B | 0.018±0.003 | 0.0088 | 0.0178 | 0.0121 | 0.0164 | 0.0180 | 0.0236 | 0.0204 |
| | G | 0.010±0.003 | 0.0039 | 0.0104 | 0.0067 | 0.0097 | 0.0105 | 0.0128 | 0.0130 |
| | R | 0.007±0.003 | 0.0021 | 0.0071 | 0.0045 | 0.0072 | 0.0073 | 0.0080 | 0.0093 |
| | N | 0.008±0.006 | 0.0025 | 0.0060 | 0.0046 | 0.0063 | 0.0063 | 0.0063 | 0.0170 |
| Aerosol radiative efficiency | B | 0.070 | 0.093 | 0.097 | 0.091 | 0.090 | 0.106 | 0.119 | 0.068 |
| | G | 0.048 | 0.037 | 0.052 | 0.043 | 0.046 | 0.057 | 0.058 | 0.041 |
| | R | 0.039 | 0.020 | 0.034 | 0.028 | 0.031 | 0.037 | 0.032 | 0.030 |
| | N | 0.052 | 0.027 | 0.029 | 0.031 | 0.031 | 0.033 | 0.028 | 0.046 |

¹ Uncertainties for MISR spectral AOD are calculated by $20\% \times \text{AOD}$ based on *Kahn et al.*[2005].

Uncertainties of $d\alpha$ are from this study. Absolute uncertainties for SSA, AE, and BHR are not yet known, due to the difficulty in obtaining validation data.

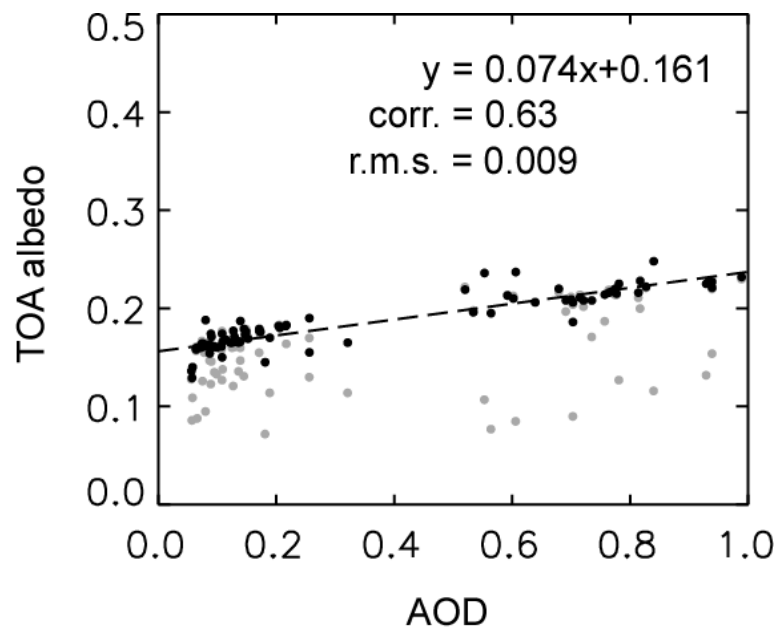


Figure 1.

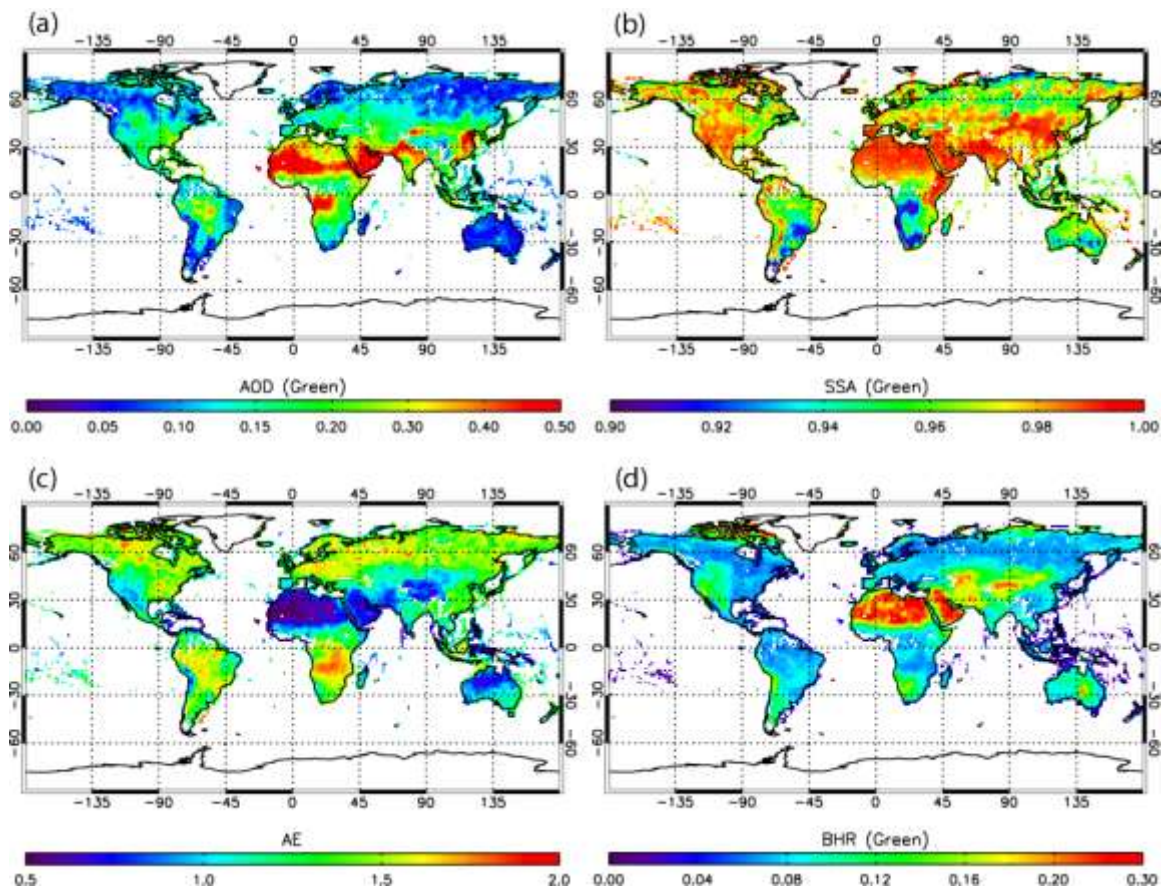


Figure 2.

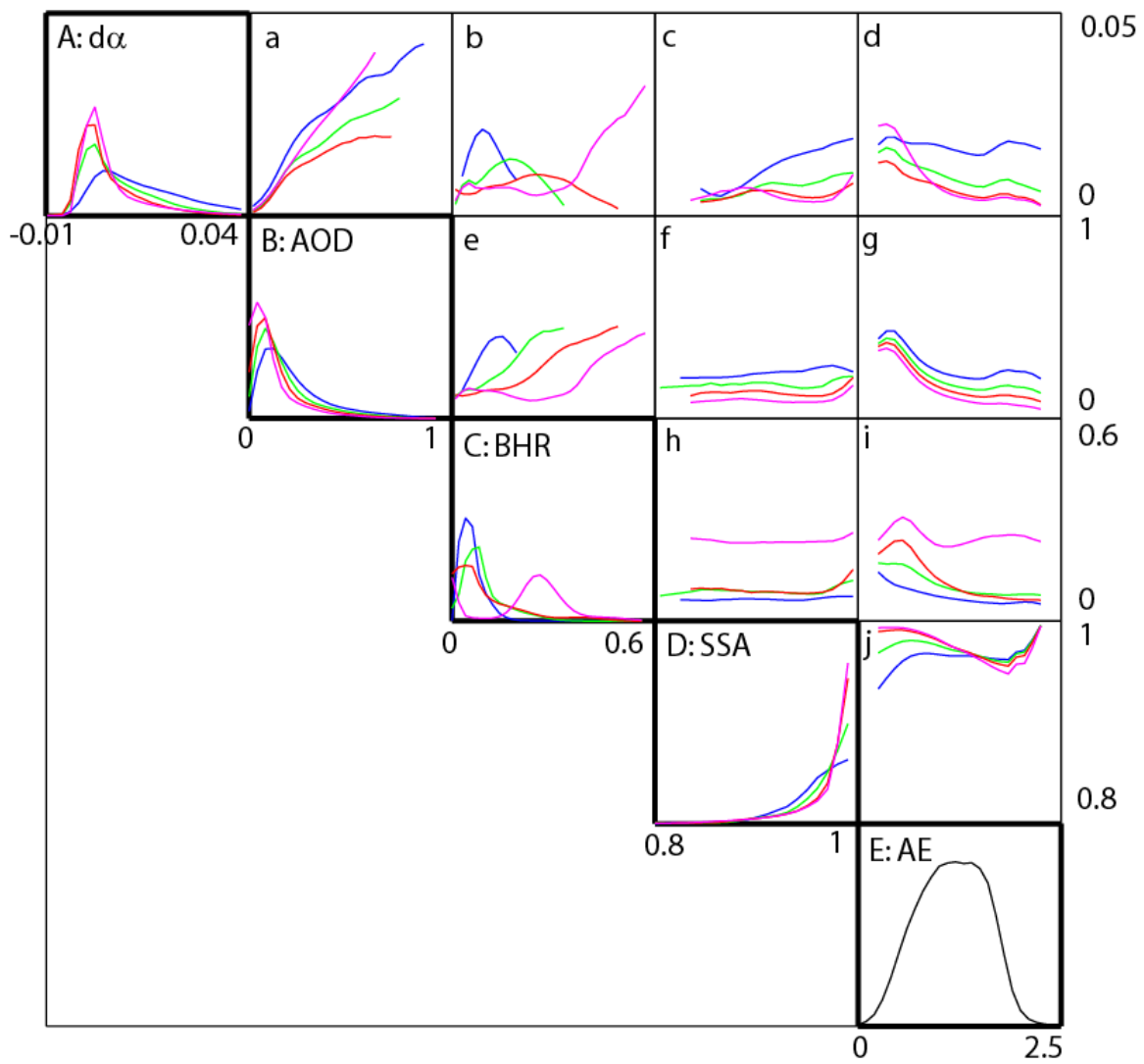


Figure 3.

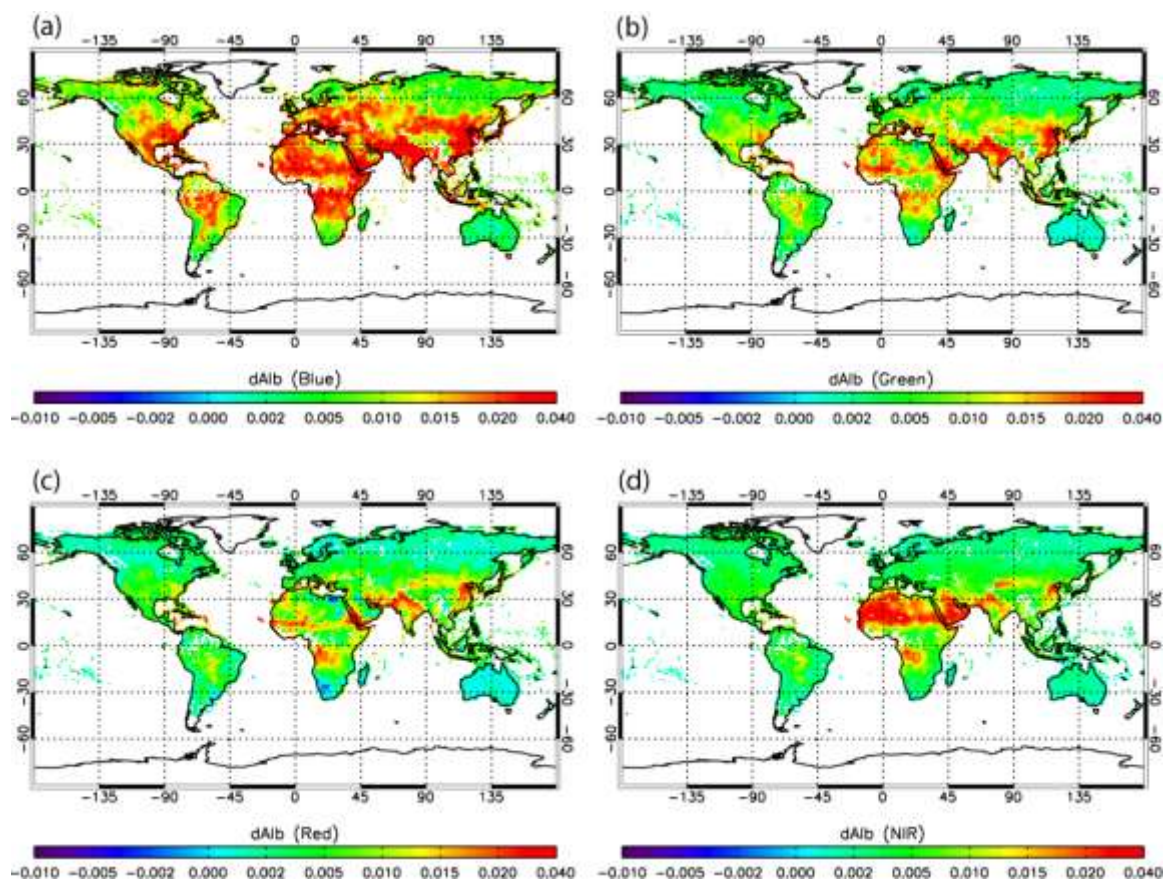


Figure 4.

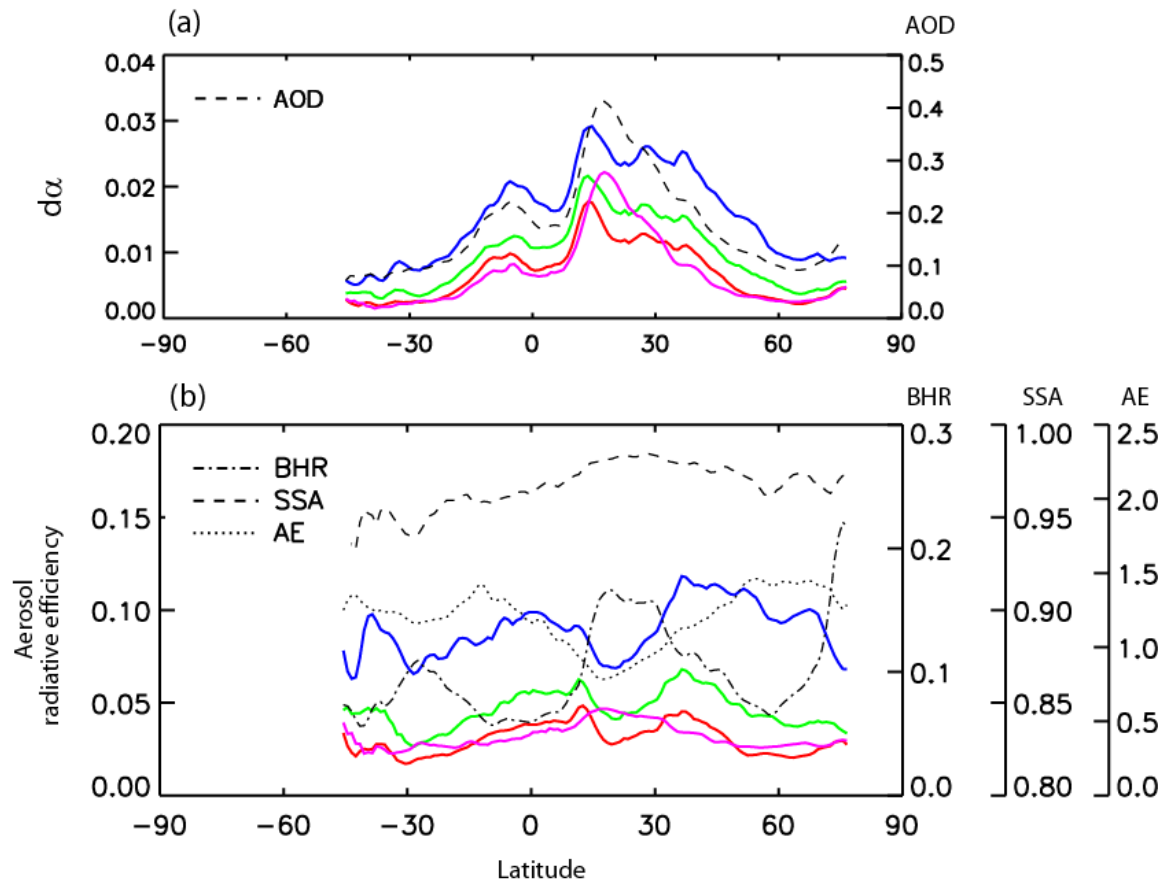


Figure 5.

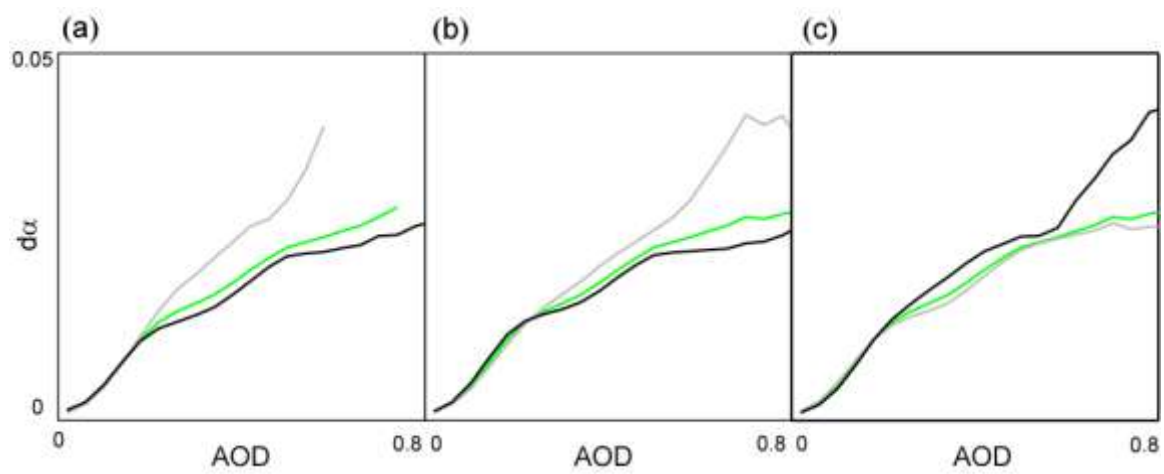


Figure 6.

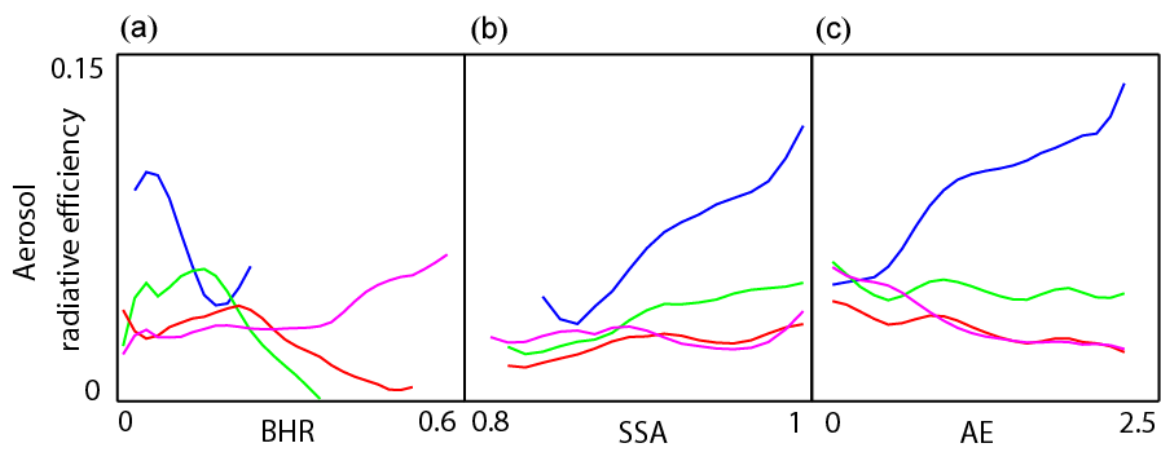


Figure 7.

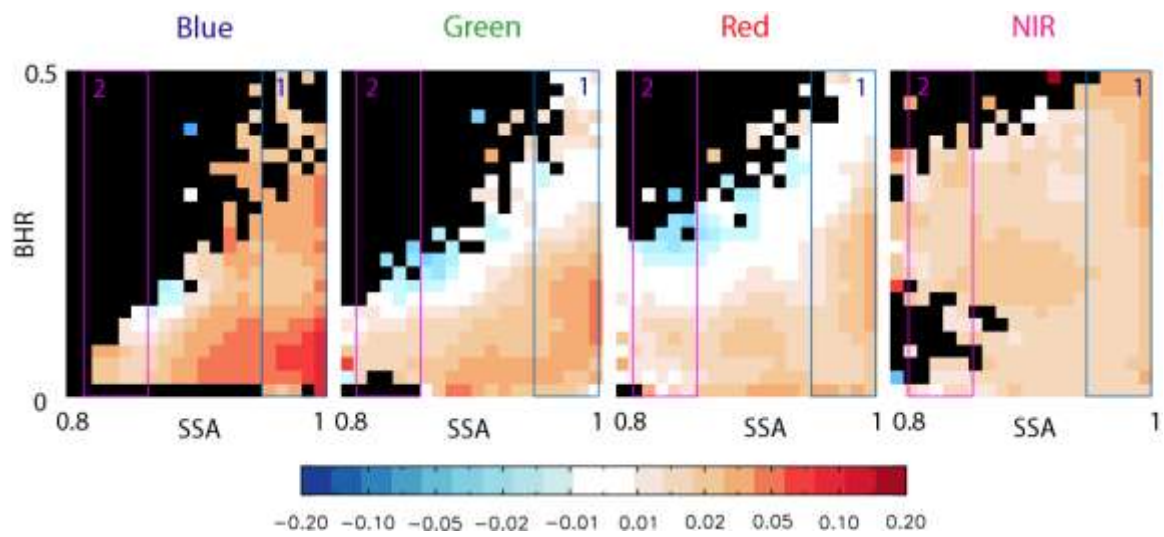


Figure 8.

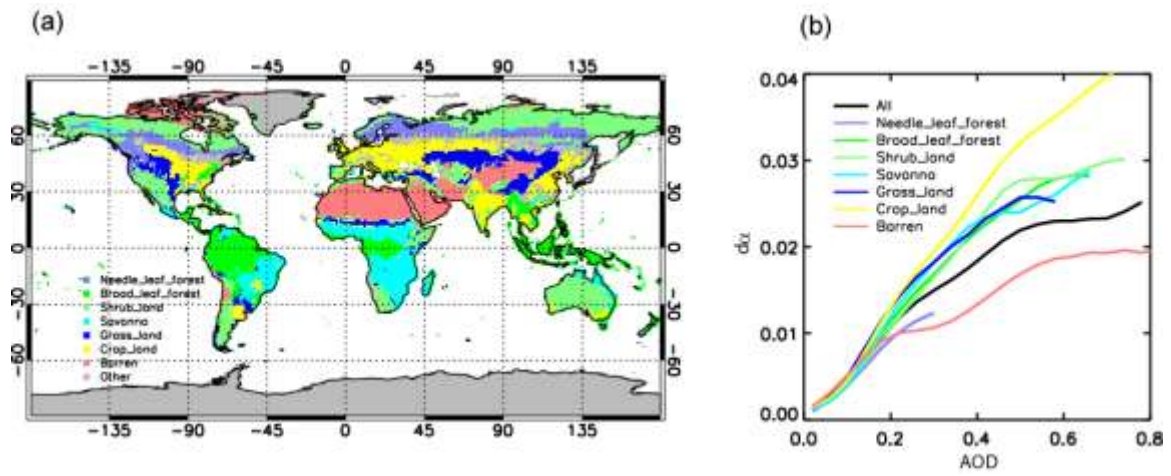
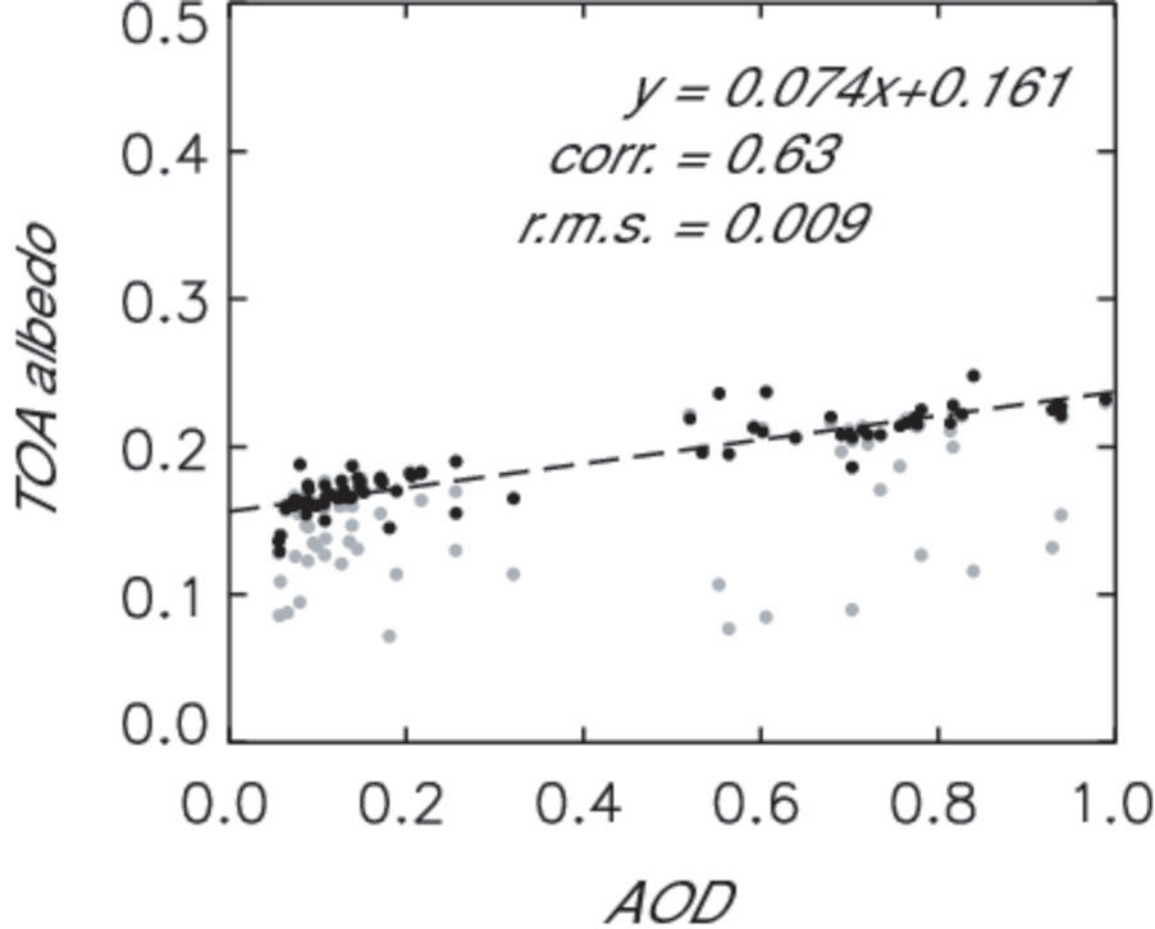
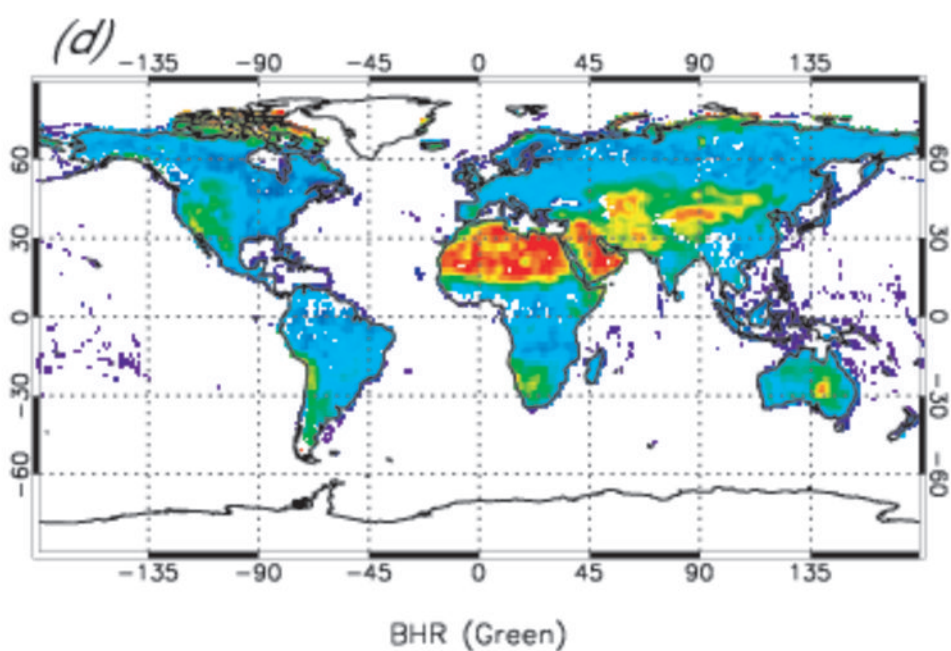
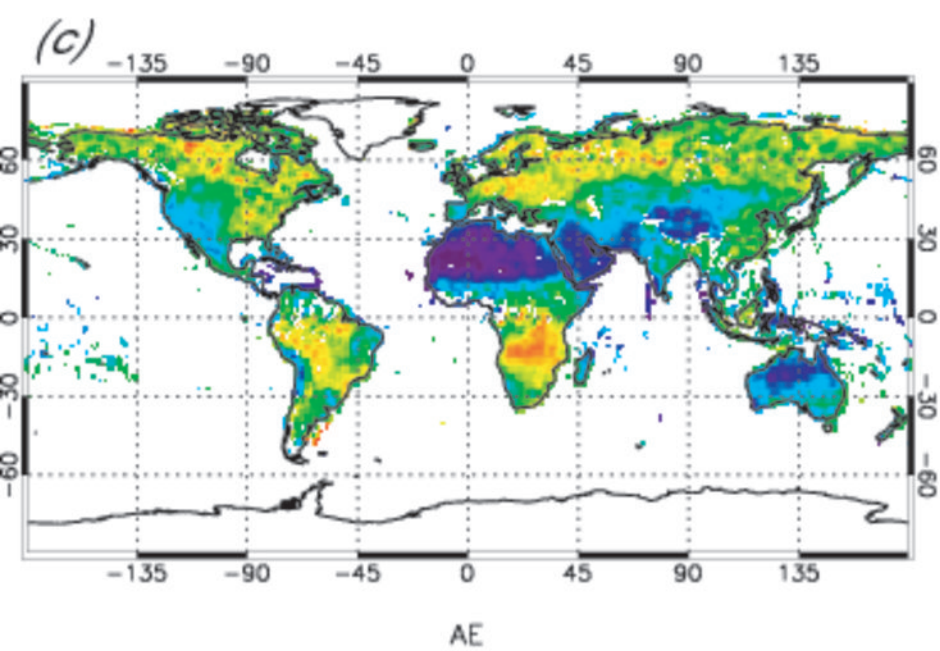
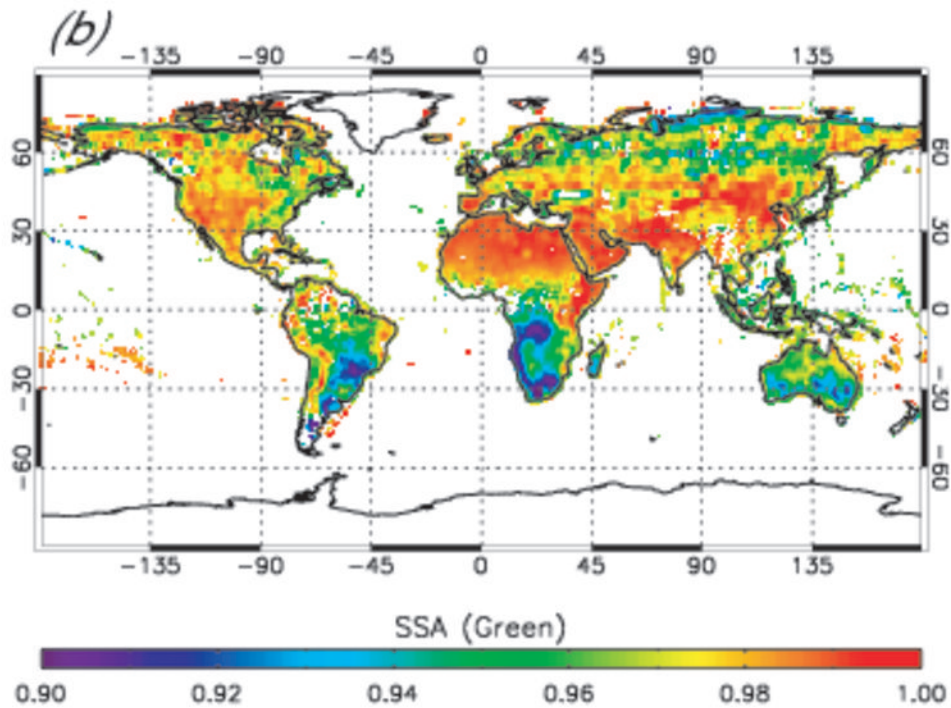
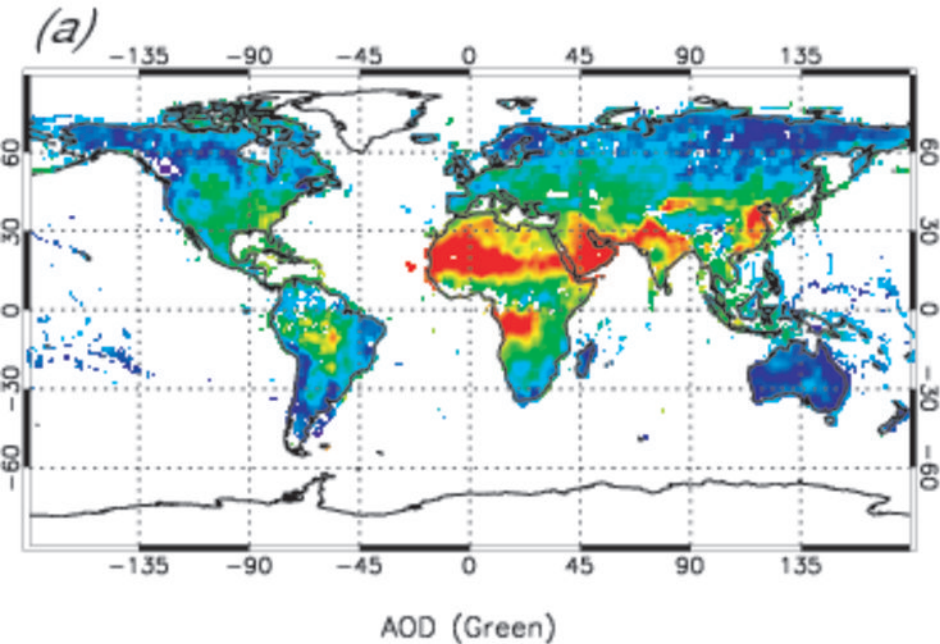
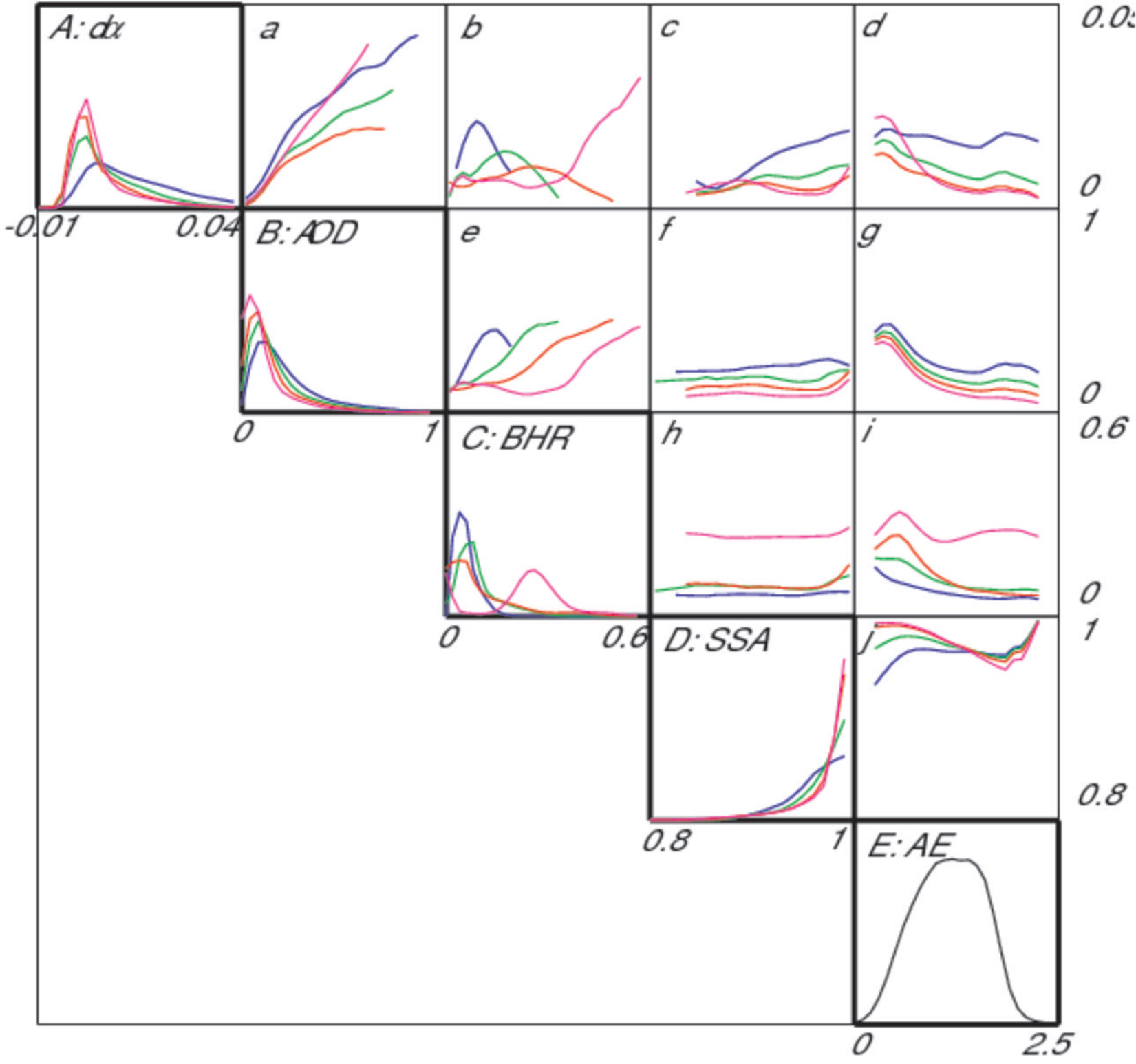
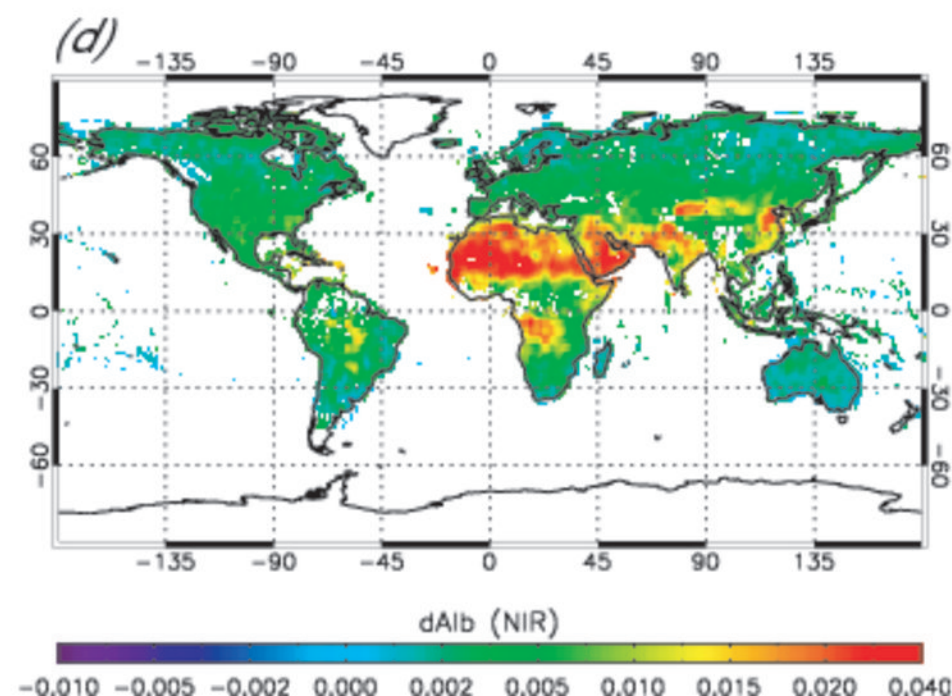
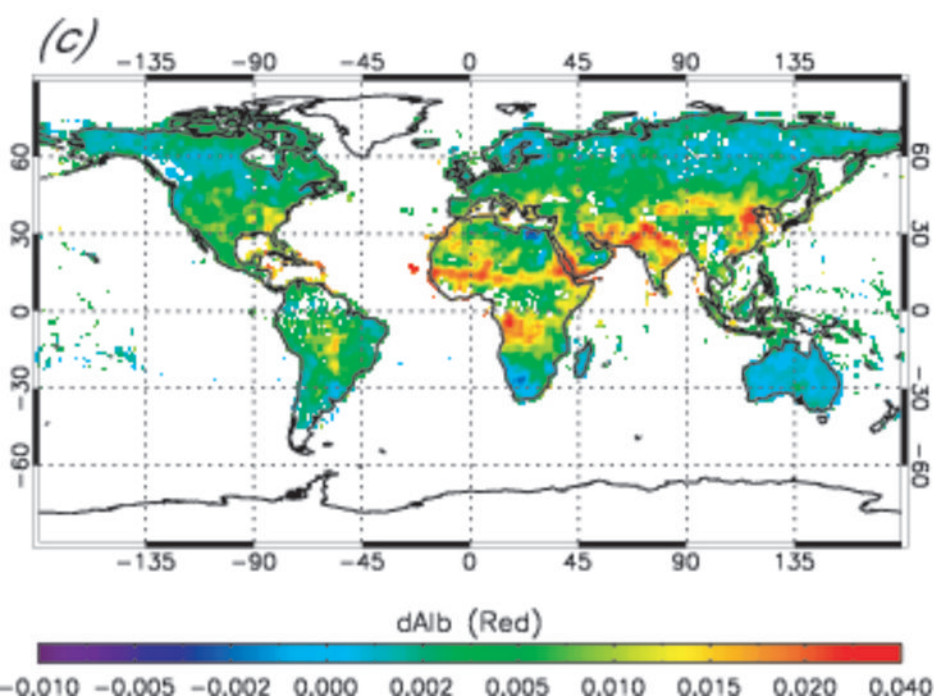
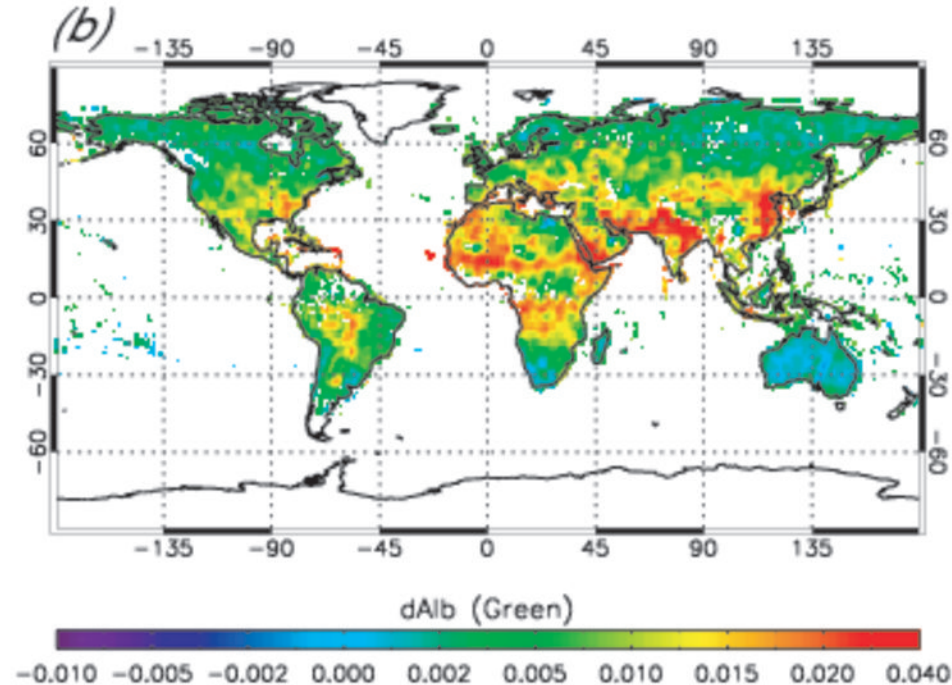
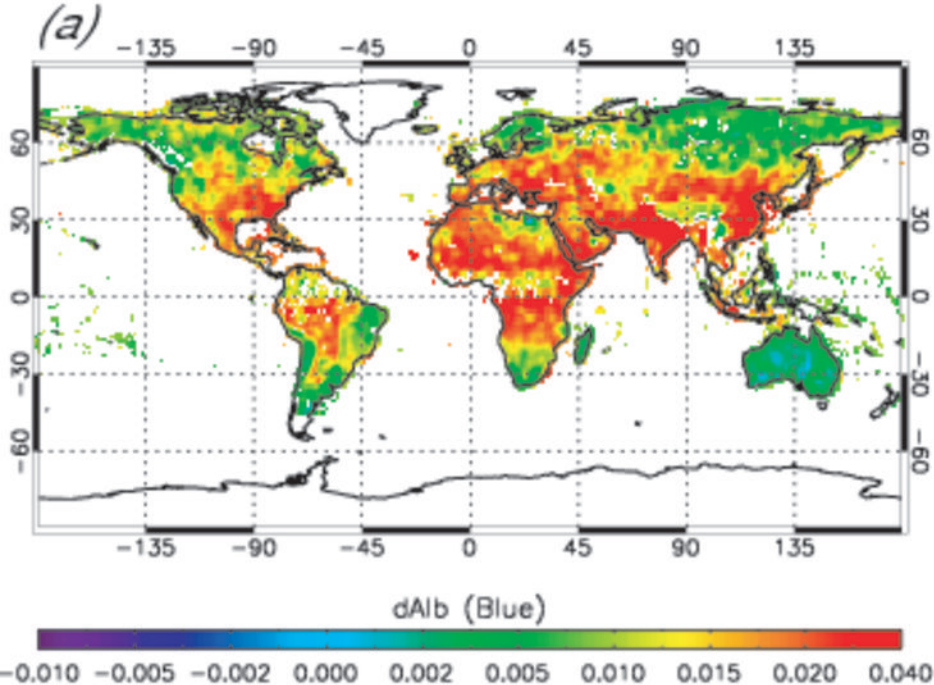


Figure 9.

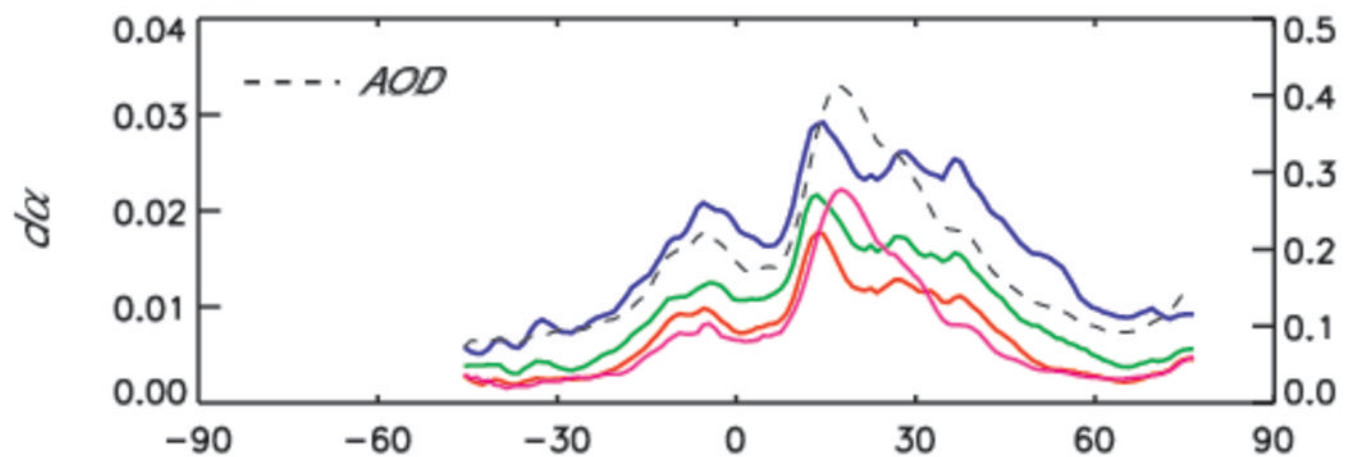








(a)



(b)

